A Low Noise Lifetime Measurement of Electrons Drifting in Liquid Argon

by

Shawn Bishop

B.Sc., McMaster University, 1995.

A Thesis Submitted in Partial Fulfillment of the
Requirements for the Degree of

MASTER OF SCIENCE

in the Department of Physics and Astronomy.

We accept this thesis as conforming
to the required standard.

Dr. R. Keeler, Co-Supervisor (Department of Physics and Astronomy)

Dr. R. Sobie, Co-Supervisor (Department of Physics and Astronomy)

Dr. M. Lefebvre, Departmental Member (Department of Physics and Astronomy)

Dr. D. Harrington, Outside Member (Department of Chemistry)

Co-Supervisor: Dr. R. Keeler

Co-Supervisor: Dr. R. Sobie

Abstract

A specially designed cryostat apparatus was built to operate a liquid argon ionization cell with very low acoustic noise. The cryostat was equipped with a system to damp out low frequency vibrations, and thus, reduce induced acoustic noise on the data transients.

A liquid argon ionization cell was tested in the new cryostat by measuring the ionization of the argon by cosmic ray muons. Digital filtering of the individual data transients improved the purity of the data set used to generate ensemble averaged transients for different electric fields across the ionization cell. Transient waveform analysis was used on these averaged transients to extract the mean electron lifetime of the ionization electrons drifting in the liquid argon. A result for the free electron lifetime of $\tau_l = \left(0.897 \pm 0.005\ (\text{stat.})\ ^{+0.023}_{-0.032}\ (\text{syst.})\right)\ \mu\text{s}$ was found.

The electron lifetime can be used as to determine the concentration of oxygen equivalent contamination in the liquid argon of this experiment. This value of the electron lifetime corresponds to a concentration of oxygen equivalent contamination of, $[O_2] = \left(748 \pm 150\ (\text{stat.})\ ^{+186}_{-125}\ (\text{syst.})\right)$ [ppb], at an applied electric field strength of 500 V/cm.

Examiners:

Dr. R. Keeler, Co-Supervisor (Department of Physics and Astronomy)

Dr. R. Sobie, Co-Supervisor (Department of Physics and Astronomy)

Dr. M. Lefebvre, Departmental Member (Department of Physics and Astronomy)

Dr. D. Harrington, Outside Member (Department of Chemistry)

Contents

List of Tables

List of Figures

Acknowledgements

For those people "behind the scenes" of this work. I take the opportunity of having this section to have *fun* in thanking each and every one of them, in turn, for the help, guidance, and understanding they gave me along the path of this project.

Paul Poffenberger: A man of few words who lets his uncanny mastery of the lab and experiment speak for him. I thank you for your many hours spent in the lab with me helping me "tame the beast". That first ever cosmic ray pulse, 80 mV in height, from the experiment we both saw together was sweet indeed.

Mark Lenckowski: An artist and a wizard. For the artist, I thank you for your technical and schematic drawings that are in this work. For the wizard, I am indebted to you for your ingenuity, and mastery of the plasma welder. You pulled *much* more than any rabbit out of the hat the day you restored the knife-edge on the LAr dewar: you saved this project.

Paul Birney: A technician's technician; exacting and precise, yet always flexible with new ideas. I thank you for designing the LAr cell, and for the technical drawings of it contained in this thesis. I also thank you for your hours of patience, guidance, and assistance in helping me learn the use and operation of the various equipment used in making this experiment operational. Drawing off your experience prevented me from having to "re-invent the wheel" when it came to operating and learning the equipment. It also prevented me from wreaking havoc with it, and making Richard very unhappy.

Peter Ward: Thanks go to the man who took my sketches for the design of the stand and pulley arrangement for the apparatus, and turned them into the real thing. And, despite all the personal and professional rough spots I encountered along the way in my time on this project, thanks for the jibing and bantering that went on between us. Indeed, there will be no more *"surfing"* outings for me along the west coast. Cheers, Mate.

Richard Keeler: The *SUPERVISOR*. First, some words: loyalty, confidence, respect, fairness, trust, and freedom. Since the summer of 1993; my first NSERC position here in the department, you have continually stood by me in my efforts to succeed in physics, and continue to do so now, even as I prepare to possibly explore other avenues of physics research. You treated me with confidence at times when I had serious doubts, and always gave me and my ideas for this project respect. During the personal rough spots in my three years here, you gave me fairness, understanding, and the space I needed to deal with them. You gave me your implicit trust to competently conduct myself in the lab with thousands of dollars worth of equipment without blowing it, Paul, or myself up. Finally, there comes freedom: the freedom to have chosen this project; freedom to make my own mistakes and learn on my own from them; freedom to explore in a hands-on way the beauty of personal discovery, and research advancement from the labours of my hard work and efforts; freedom in being given the chance to contribute to undergrad teaching; and finally, being given the freedom to take on political endeavours well outside the realm of physics: CUPE 4163. Kudos to you Richard.

For the perseverance, strength, and determination, that go part and parcel with completing a work of this magnitude:

To Mom.

Glossary of Abbreviations

ADC: Analog to Digital Converter.

ATLAS: A Toroidal LHC ApparatuS.

atm: Atmosphere.

CAMAC: Computer Automated Measurement And Control.

CERN: European Centre for Nuclear Research.

DAQ: Data AcQuisition.

DP: Digitization Point

DF: Digital Filter

FPH: Filtered Pulse Height(s).

HV: High Voltage.

LAr: Liquid Argon.

LArCal: Liquid Argon Calorimetry.

LHC: Large Hadron Collider.

LN_2: Liquid Nitrogen.

NIM: Nuclear Instrument Module.

ppb: Parts Per Billion.

Transient/Waveform: Voltage pulse obtained from the liquid argon ionization cell. Both words are used interchangeably throughout this work.

Chapter 1

Introduction

Liquid argon calorimetry (LArCal) will play a crucial role at the ATLAS experiment at the LHC project currently under construction at CERN. Calorimeters offer the advantage of an intrinsic energy resolution that improves with increasing particle energy. Additionally, LArCal also has relatively fast signal rise times which will help to reduce the level of overlapping signal events in experiments with high luminosity, such as LHC. Finally, liquid argon has the property of being radiation hard; an important property for high luminousity environments such as those at the LHC. Argon, a noble gas, is only subject to damage due to nuclear reactions; this in contrast to scintillator type calorimeters which are prone to radiation damage due to chemical alterations. Liquid argon, however, has the inconvenience of being a cryogenic material, requiring the need for complicated cooling and heat exchanging systems on large experiments such as ATLAS, and as a result, some portions of the active volume of detectors are used for housing cryogenic components.

A high energy charged particle, as it traverses through liquid argon, will ionize the argon atoms through collisions, producing free electrons and Ar^+ ions. The free electrons, with the application of an external electric field, will then be able to drift through the liquid argon at a constant drift velocity, v_d, in manner analogous to a

semi-conductor device. The performance of LArCal can be degraded by the presence of contaminant molecules dissolved in the liquid argon. Electronegative species such as O_2 and N_2, and the halogens, can seriously degrade the performance of a calorimeter by trapping the free electrons thereby preventing the full electronic signal from being measured. Tests for the level of contamination in a LAr sample can be performed by making a measurement of the electron lifetime, τ_l. Tests for this have been done in the past with ultrapure, few parts per billion, liquid argon [1]. Detecting small concentrations of contaminants requires low levels of electrical and acoustical noise on the signal transient. Traditional methods in experiments of this nature have involved cryogenic techniques, maintaining the liquid argon at 86 K[1], that have been inherently "noisy", making low noise measurements of the electron lifetime difficult to achieve. These methods typically consist of using a pressurized liquid nitrogen (LN_2) bath, or LN_2 circulation technique. The LN_2 boiling point is 77 K at one atm and therefore, it must be pressurized to 2.4 atm to raise its temperature to 86 K, appropriate for maintaining argon liquid. Both cooling techniques produce sources of noise; from the high pressure venting of evaporated nitrogen gas, in the case of the bath technique, and from vibrational motion, in the case of the circulation technique. The pressurized dewars containing the LN_2 are also an additional experimental difficulty.

In this experiment, we use a refrigeration technique to condense, and maintain liquid argon at 86 K. This method offers the clear advantage of more flexible user control of the experiment, by virtue of being able to quickly turn the refrigerator on or off as the experimenter chooses. It also eliminates the need of a constant supply of LN_2. The refrigeration technique makes the experiment more readily modified, as

[1]The boiling point of argon is $\approx$ 87.5 K, and the melting point is $\approx$ 84 K, in equilibrium. We choose 86 K as it provides a safe temperature margin between these two critical temperatures.

its accessibility is improved by removing the need to have the LAr dewar immersed in a LN_2 bath. However, like the other techniques, refrigeration also has problems associated with acoustic noise caused mainly by mechanical vibrations from the piston cycle of the cryo-cooler that are transmitted into the LAr ionization cell inducing noise signals on the output waveforms from the cell. To be able to effectively utilize a self-contained refrigeration technique, then, requires isolating the experimental cell from the mechanical vibrations caused by the cryogenic cooler.

This thesis demonstrates that a prototype cryostat apparatus, employing a self-contained cryogenic refrigeration system, is able to effectively decouple the experimental cell from the mechanical vibrations of the cryo-cooler. Transient waveforms, from ionization caused by cosmic ray muons, were recorded using a single charge integrating preamplifier. In contrast to previous measurements, further online filtering of the data was not needed. This allowed data to be taken with a much broader electronic bandwidth, and in principle, with less systematic effects from distortions caused by additional filtering.

Chapter 2 of this thesis presents the theoretical groundwork to describe the nature of the current and voltage transients that arise from the passage of a charged particle through an ionizing medium in a parallel plate ionization cell. The output voltage transient is a convolution of the current pulse produced from the cell with the impulse response of the electronics. The model used to describe the electronics is presented and its impulse response is derived. Cosmic ray muons are used as the source of ionization in this experiment. The spectrum of cosmic ray muons at sea level and the Bethe-Bloch theory of charge deposition from an ionizing particle traversing an ionization medium are presented.

Chapter 3 outlines the construction, design and mounting of the cryostat appa-

ratus, including a section on vibration damping. We describe the design and preparation of the liquid argon ionization cell, and the procedure employed for condensing argon gas in it. The data acquisition system is discussed, and the experimental run procedure is described.

In chapter 4 we present the data analysis, beginning with the analysis of the measured electronic impulse response function. A digital filter, used in distinguishing signal from background events, is discussed, and developed, including its optimization for use on the data sets of this experiment. The selection cuts imposed on the data sets are then discussed, and their application to the procedure for determining the free electron lifetime is presented.

Chapter 5 summarizes the results obtained for the free electron lifetime, the ratio of the average charge collected between the two ionization cells used in this experiment, and finally the concentration of oxygen equivalent contaminants in the liquid argon. The theoretical fits to the data are presented, and systematic errors and corrections are discussed.

Chapter 6 summarizes the results of this work and discusses what conclusions can be drawn from them. In addition, some proposals on how future experiments of this nature can be improved beyond what was done in this work.

Chapter 2

Theory

This chapter presents the theoretical derivation of the mathematical form of the LAr transients that are expected from the parallel plate ionization cell used in this experiment.

We use the result derived in Appendix C for the surface charge on a grounded plate of a parallel plate capacitor, induced by a point charge located between the two plates, to derive the detected charge in a circuit connecting the two plates. This result is used to derive the current in the circuit between the plates, followed by a discussion on how this current is altered due to electron trapping by electronegative impurities in the liquid argon. These results are combined using linear circuit theory to arrive at the mathematical wave form of the LAr voltage transient which is used to fit the data obtained from the experiment.

Finally, we conclude this chapter with a discussion of the ionization energy loss of a muon using the Bethe-Bloch theory, and discuss the implications of this for the experiment.

2.1 Ionization Chamber Current

Equation C.6 gives the charge induced on a grounded plate of a parallel plate capacitor by a positive point charge located between the two plates:

$$q_I = +q\left(\frac{z}{L} - 1\right) , \tag{2.1}$$

where L is the separation of the plates and z is the location of the charge, $+q$, between the plates. Consider a line of negative charge, initially of length R, deposited uniformly between the plates, by the passage of an ionizing particle, as depicted in figure 2.1, and its subsequent upward displacement toward the ground plate, S_1, located at $z = 0$. We assume a uniform negative line charge density, λ, of,

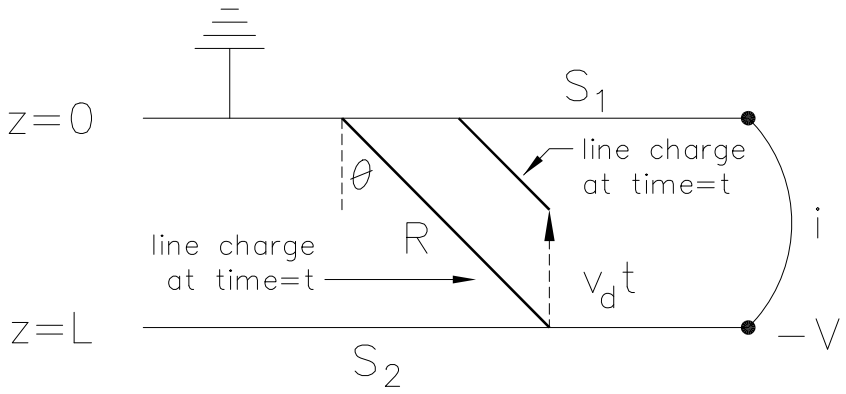

Figure 2.1: Ionization chamber track configuration The line of negative charge of length R is initially deposited by the passage of the ionizing particle through the cell. At some later time, t, the line of charge has translated a distance $v_d t$ upward toward the collection plate located at $z = 0$.

$$\lambda = \frac{-Ne}{R} = \frac{-Ne}{L}\cos\theta , \tag{2.2}$$

where e is the fundamental unit of electrical charge[1], N is the total number of initial negative charges, and R is the total length of the initial line of charge.

[1]We adopt the convention $e > 0$ throughout this work.

After a time $t < t_d$, the line of charge translates a vertical displacement of $v_d t$ towards the upper ground plate, where v_d is the constant drift velocity of the electrons, and t_d is the total time for an electron to drift across the gap width, L. The induced charge, q_I^-, on the ground plate caused by the line of negative charge at time t is then,

$$q_I^-(t) = \int_0^{R-\frac{v_d t}{\cos\theta}} \lambda \left(\frac{r\cos\theta}{L} - 1 \right) dr \,, \tag{2.3}$$

where we have used equation 2.1, with $z = r\cos\theta$. Performing the integration yields for q_I^-:,

$$q_I^-(t) = -\frac{Ne}{2}\left[\left(\frac{v_d t}{L} \right)^2 - 1 \right] = -\frac{Ne}{2}\left[\left(\frac{t}{t_d} \right)^2 - 1 \right] . \tag{2.4}$$

Note that the $+Ne/2$ term in equation 2.4 is simply the result of the charge induced on S_1 by the initial negative line of charge prior to any displacement; that is, at $t = 0$.

In the case of this experiment, the situation is actually more complicated. Instead of a single negative line charge, cosmic ray muons traversing through the liquid argon leave a track of electron-ion pairs. Thus, there is a negative and positive line charge. When the integration is performed over the line charge of positive ions, one will get $q_I^+ = -Ne/2$ as the total charge induced on S_1, from the positive ions. The result is that these two initial values from each line of charge will cancel out. As the mobility of Ar^+ ions is several orders of magnitude lower than that of electrons, the line of positive charge from the Ar^+ ions can be assumed to be effectively at rest over the time duration it takes for all the electrons to drift across the gap. Therefore, there is no time dependence of the induced charge on S_1 from the argon ions.

Lastly, there is the amount of charge being directly absorbed onto S_1, q_{abs}^-. In

the time t, we have,

$$q^{-}_{abs} = \lambda \frac{v_d t}{\cos\theta} = -Ne\frac{v_d t}{L} = -Ne\frac{t}{t_d} \tag{2.5}$$

as the amount of charge absorbed on S_1.

The net charge in the wire connecting S_1 and S_2, Q, is then the sum of all the terms; $q_i^{\pm}$ and q_{abs}. The $\pm Ne/2$ terms from the initial line charge contributions cancel, leaving us,

$$Q = Ne\frac{t}{t_d}\left(1 - \frac{t^2}{2t_d}\right) \tag{2.6}$$

as the detected charge in the circuit between the two plates. The current flowing in the wire between the plates, $i(t)$, is just the time derivative of equation 2.6, and is,

$$i(t) = \frac{dQ}{dt} = \frac{Ne}{t_d}\left(1 - \frac{t}{t_d}\right) . \tag{2.7}$$

Throughout the above calculations it is assumed that the uniformity of the line charge will remain preserved over the course of the entire drift time. The liquid argon diffusion coefficient, D, for the electric fields used in this experiment is $\approx 15\,, \mathrm{cm^2 s^{-1}}$ [16]. The rate of diffusion, $d\langle r\rangle/dt$ is,

$$\frac{d\langle r\rangle}{dt} = \frac{1}{2}\left(\frac{D}{t}\right)^{\frac{1}{2}} , \tag{2.8}$$

where $\langle r\rangle$ is the mean spread in position away from the original line of charge. The diffusion rate is only of order $5\,\mathrm{m/s}$ while the drift velocity, however, is of order $10^3\,\mathrm{m/s}$; almost three orders of magnitude higher. As a result, over the course of the drift time, $t_d = 10\,\mu\mathrm{s}$ the electron line charge will essentially remain uniform for the purposes of the preceding calculations.

2.1.1 Attenuation of the Detected Current

As electrons migrate across the cell gap, some will be captured on electronegative impurities. As a result, these contaminants within the argon will cause attenuation of the signal current. These contaminant atoms will have mobilities comparable to that of the Ar^+ ions, and can therefore be treated as being stationary over the course of the electron drift time, t_d. We can characterize this capturing process by the reaction equation:

$$e^- + X \longrightarrow X^- \,, \tag{2.9}$$

where X represents an electronegative species within the liquid argon. The rate equation for the concentration of free electrons, n, is then,

$$\frac{dn}{dt} = B[X^-] - C[X]n \,, \tag{2.10}$$

where B is the reaction rate for the dissociation of X^- into its constituents and C is the reaction rate for the formation of X^-. Here, the [ ] denote concentrations of the respective species. Once electrons are bound to an electronegative species, they remain trapped for the duration of the electron drift time, whence, $B = 0$. With this condition the number of free electrons, $N(t)$, which is proportional to the concentration of free electrons, is,

$$N(t) = N(0)\, e^{-t/\tau_l} \,, \tag{2.11}$$

where $\tau_l \equiv (C[X])^{-1}$.

The time dependence of the detected current arises as a result of the kinematics of the free electrons moving across the cell gap. At each "snapshot" in time, the number of drifting electrons will have decreased due to capture, but their kinematics

remains unchanged. This effect allows one to use the result of equation 2.11 to modify equation 2.7 to give the final form of the current in the wire between the two plates as:

$$i(t) = \begin{cases} \frac{N(0)e}{t_d}\left(1 - \frac{t}{t_d}\right) e^{-t/\tau_l} & , \; t \leq t_d \\ 0 & , \; t > t_d \end{cases} . \tag{2.12}$$

Equation 2.12 describes the expected current in the amplifier circuit of the experiment. Notice, the effect of the trapping of the electrons effects the *shape* of the measured current pulse. This shaping effect caused by the contamination is clearly seen in figure 2.2, where normalized plots of equations 2.7 and 2.12 are shown.

2.2 LAr Voltage Transient

For a general circuit consisting of linear elements the voltage output of the circuit to a known input current, $i(t)$, is the convolution of the current with the impulse response function, $h(t)$ of the system [2, 8];

$$V(t) = \int_0^t i(t-\xi)h(\xi)\,d\xi = \int_0^t i(\xi)h(t-\xi)\,d\xi\,. \tag{2.13}$$

Further, the impulse response function of a system, $h(t)$, is simply the output the system gives when the input current is a delta function, $\delta(t)$.

We model the charge integrating preamplifier, as depicted in figure 2.3, as an RC integrator followed by an RC differentiator [9], with characteristic time constants, τ_1 and τ_2, respectively. The oscilloscope used to digitize the signal transients is modelled as a perfect integrator. The reasons for this are that the integration time constant of the oscilloscope is of the same order of that of the preamplifier, making it indistinguishable from the preamplifier, while the differentiation time of the oscilloscope is three orders of magnitude larger than that of the preamplifier. On the time scale that

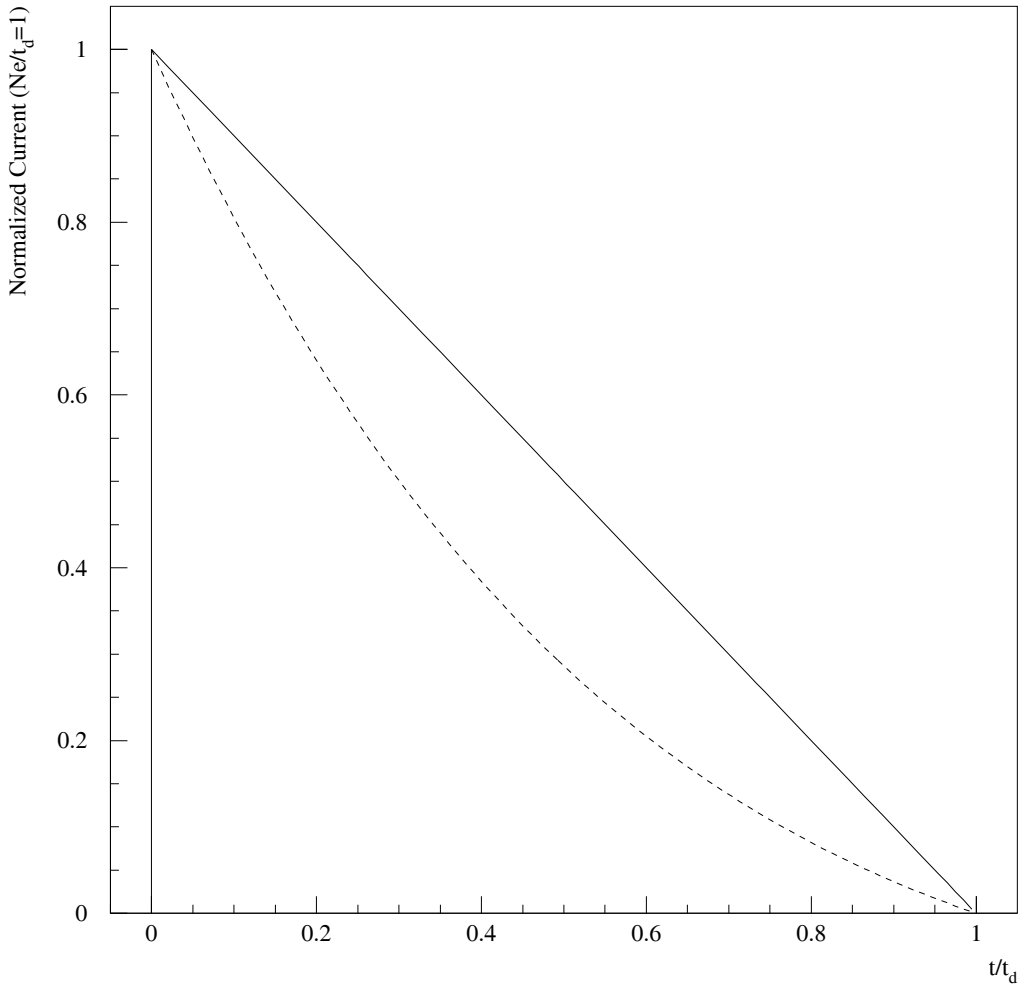

Figure 2.2: The effect of attenuation on the detected current signal. The solid line shows the detected current for a pure argon system. The dashed line shows the detected current with contamination that attenuates the signal. The dashed plot uses the lifetime determined in this work.

data was recorded for this experiment ($\approx 20\,\mu$s) , the effective differentiation time constant of the oscilloscope is infinite, with the preamplifier's differentiation time constant totally dominating the signal shaping. With these simplifications, the impulse

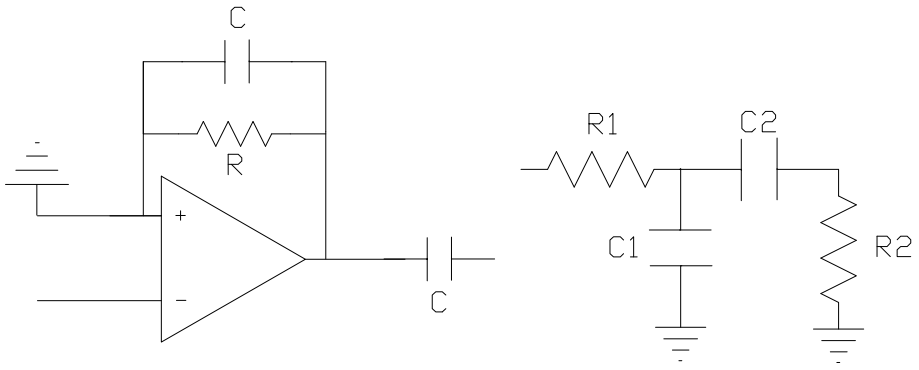

Figure 2.3: Schematic diagram depicting the model used for the preamplifier. The left side depicts the charge integrating preamplifier, which is then modelled as an RC integrator followed by an RC differentiator, as shown on the right.

response of the oscilloscope is equivalent to a step function, $U'(t)$, with characteristic time constant τ_3, defined as:

$$U'(t) = \begin{cases} 1/\tau_3\,, & t \geq 0 \\ 0\,, & t < 0\,. \end{cases} \tag{2.14}$$

Using Laplace transform analysis [2] for the circuit components depicted in the right half of figure 2.3, and treating the oscilloscope as a perfect integrator as explained above, the impulse response function is derived to be,

$$h(t) = \frac{\tau_2}{\tau_3(\tau_2 - \tau_1)}(e^{-t/\tau_2} - e^{-t/\tau_1})\,. \tag{2.15}$$

Inserting this form for the impulse response, and the current signal of equation 2.12, into equation 2.13, and performing the integration, yields a form for the LAr voltage transient of,

$$V(t) = \begin{cases} \beta \sum_{i=1}^{2} \frac{(-1)^{i+1}}{(\alpha_i t_d)^2} \left\{[\alpha_i(t_d - t) - 1]e^{-t/\tau_l} + (1 - \alpha_i t_d)e^{-t/\tau_i}\right\} & ,\ t \leq t_d \\ \beta \sum_{i=1}^{2} \frac{(-1)^{i+1}}{(\alpha_i t_d)^2} \left(1 - \alpha_i t_d - e^{-\alpha_i t_d}\right) e^{-t/\tau_i} & ,\ t > t_d \end{cases} \tag{2.16}$$

where β and α_i are given by,

$$\beta = G\frac{Ne\tau_2}{\tau_3(\tau_2 - \tau_1)}\,, \tag{2.17}$$

and

$$\alpha_i = \frac{\tau_i - \tau_l}{\tau_i\tau_l}\,,$$

where G is the preamplifier gain. Figure 2.4 shows $V(t)$ for values of the lifetime and characteristic time constants obtained in this work.

2.3 Cosmic Ray Muons

Cosmic ray muons arise from pion decays, which themselves are produced via nuclear reactions from collisions of cosmic rays with the molecules in the Earth's upper atmosphere. The muons, with a typical lifetime of $2.2\,\mu$s easily reach the surface of the Earth. The flux of cosmic ray muons in the vertical direction at sea level is $90\,\mathrm{m}^{-2}\mathrm{s}^{-1}\mathrm{sterad}^{-1}$, and the overall angular distribution at sea level is proportional to $\cos^2\theta$ [5], where θ is the angle with respect to the normal at the surface of the Earth. Figure 2.5 shows the measured hard component of the cosmic ray momentum spectrum at sea level for muons arriving within 10° of vertical. The vast majority of cosmic ray particles at the surface of the Earth are muons [3], and as a result, provide the source of ionizing radiation for this experiment.

2.3.1 Ionization Energy Loss of an Ionizing Particle

As muons pass through matter, and incur collisions with the atoms of the matter, their dominant energy loss is in the form of ionization, as they dislodge atomic electrons from their parent nuclei. This process produces the free electrons in the ionization cell. The energy loss per unit track length of the incident particle, dE/dx, is given

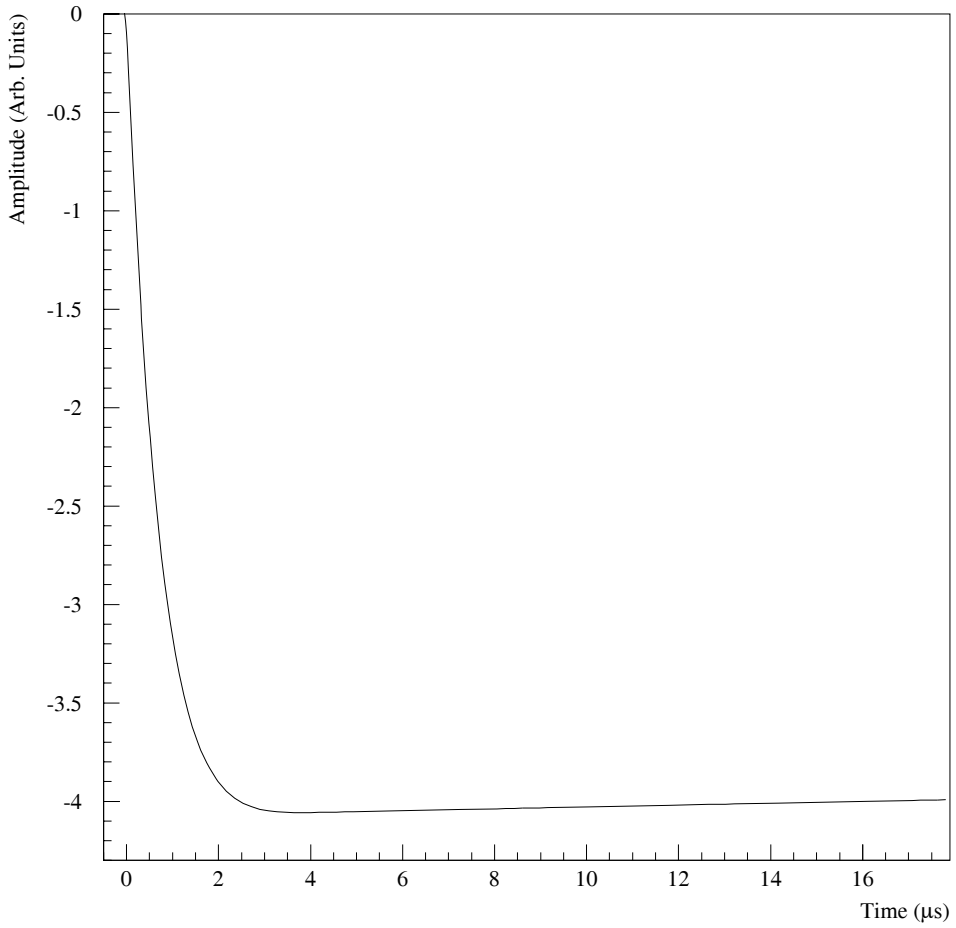

Figure 2.4: A sample theoretical LAr voltage transient of the form given in equation 2.16, with the parameters set to the values obtained in this work.

by the Bethe-Bloch equation [4]:

$$-\frac{dE}{dx} = 2\pi N_a r_e^2 m_e c^2 \rho \frac{Z}{A}\frac{z}{\beta^2}\left[\ln\left(\frac{2m_e\gamma^2 v^2 W_{max}}{I^2}\right) - 2\beta^2 - \delta - 2\frac{C}{Z}\right], \qquad (2.18)$$

where r_e is the classical electron radius, m_e is the electron mass, $N_a = 6.022 \times 10^{23}\,\mathrm{mol}^{-1}$ is Avagadro's number, c is the speed of light in vacuum, ρ is the density of the absorbing material, Z is the atomic number of the absorbing material, A is the

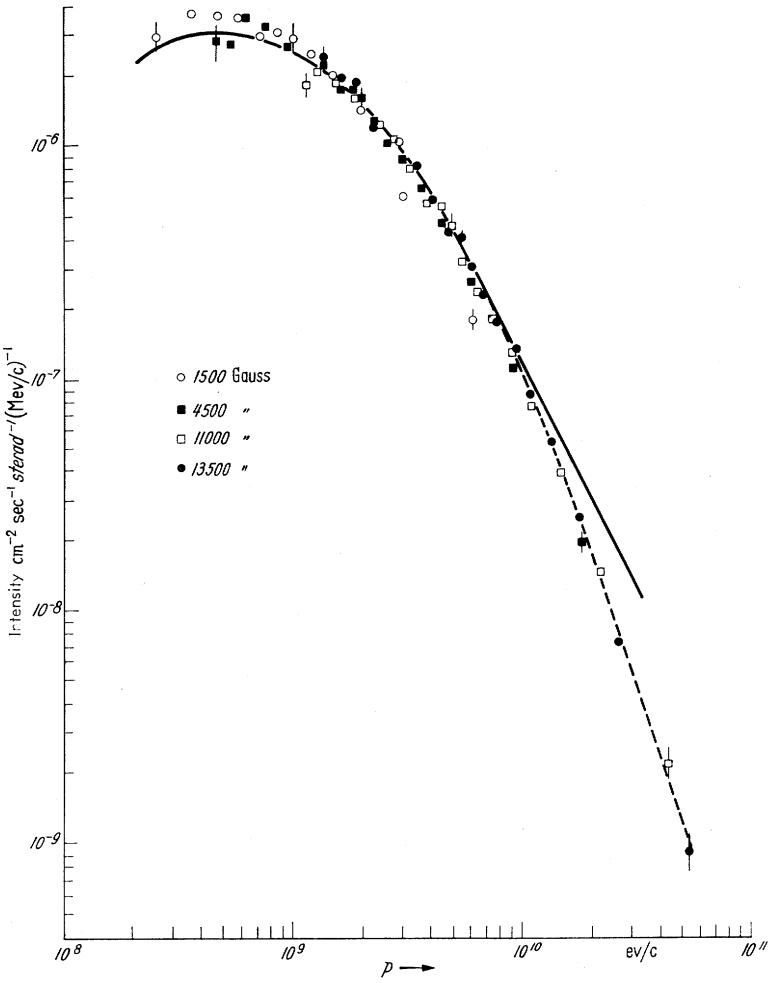

Figure 2.5: Hard component cosmic ray muon momentum spectrum as measured at sea level by a cosmic ray spectrograph. The different data points are for the listed applied magnetic fields in the spectrograph, and the lines correspond to two different theoretical fits. Source [3].

atomic weight of the absorbing material, z is the charge of the incident particle, in units of e, $\beta = v/c$ the velocity of the incident particle divided by the speed of light, $\gamma = 1/\sqrt{1-\beta^2}$, W_{max} is the maximum energy transfer in a single collision between the incident particle and a particle of the absorbing material, I is the mean excitation potential of the material, δ is the density correction, and C is the shell correction for the material. The maximum energy transfer is that produced in a head-on collision. For an incident particle of mass M, a kinematic treatment gives W_{max} as,

$$W_{max} = \frac{2m_e c^2 \eta^2}{1 + 2s\sqrt{1+\eta^2} + s^2}\,, \tag{2.19}$$

where $s = m_e/M$ and $\eta = \beta\gamma$. Figure 2.6 shows the stopping power, dE/dx, as a function of kinetic energy for an incident muon as it passes through liquid argon.

The experiment, being located in the basement of the Elliott building, has an overlying layer of concrete above it of approximately 2 m in thickness from the floors of the building. This is sufficient material thickness to ensure that the only cosmic ray muons reaching the experiment are those from the hard component of the muon energy spectrum, and that those muons reaching the experiment will also be predominantly minimum ionizing. Nuclear range data table calculations showed that a muon kinetic energy of at least 1.13 GeV is required to penetrate 2.1 m of overlying concrete. This minimum required kinetic energy is located just at the onset of the sharply falling tail from the maximum in figure 2.5.

Calculations, using nuclear range data tables for protons [6] converted to tables for muons by way of [4],

$$R_\mu(E_\mu) = \frac{m_\mu}{m_p}\left(\frac{z_p}{z_\mu}\right)^2 R_p\left(E_p\right)\,, \tag{2.20}$$

where $E_\mu = \frac{m_\mu}{m_p}E_p$ with m_μ and m_p being the masses of the muon and proton, respectively, and E_p the kinetic energy of the proton, showed that at least 300 MeV

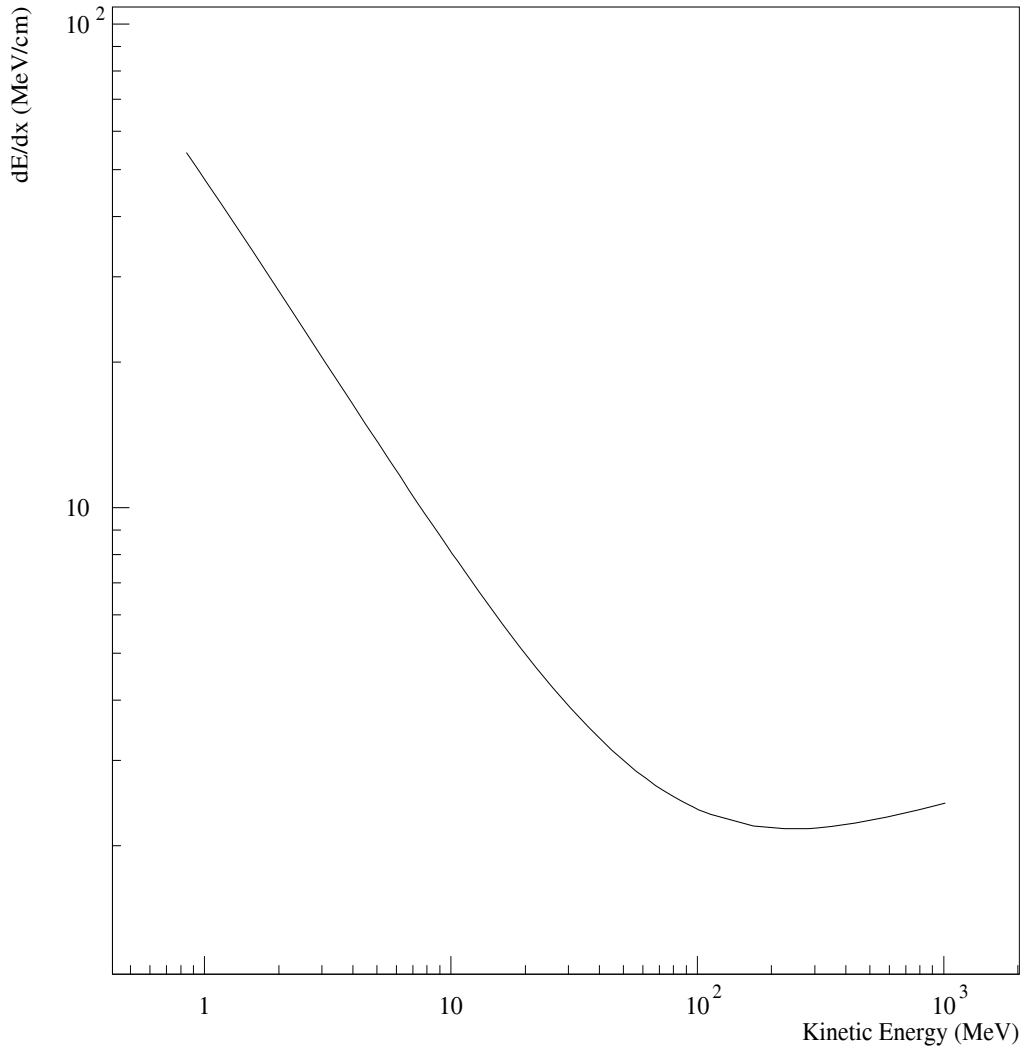

Figure 2.6: The stopping power dE/dx as a function of kinetic energy for muons passing through liquid argon. Obtained from source [6], with the original table of values for protons converted for muons according to equation 2.20.

of kinetic energy, E_μ, is required by a muon to penetrate all liquid argon and steel from the underside of the topmost plate in the ionization cell to the lower scintillator paddle. Referring to figure 2.6, we see that 300 MeV and onward corresponds to the minimum and slowly rising relativistic plateau of the dE/dx curve. The total amount of charge, Q, deposited in the liquid argon due to ionization is proportional to the dE/dx of the particle along its trajectory [7]; that is,

$$\mathcal{Q} = e\frac{L}{E_{pair}}\frac{dE}{dx}\,, \tag{2.21}$$

where L is the gap width of the ionization cell, and E_{pair} is the energy required to produce an ion pair in liquid argon. For this reason we can expect that the muons traversing through the LAr ionization cell, being hard component muons with kinetic energies in excess of 300 MeV, to produce nearly minimum ionization in the LAr cell. This feature will be important for a systematic correction in chapter 5.

Chapter 3

The Experiment

This chapter describes the experimental apparatus, and the procedures used in its implementation. The cryostat is discussed first, describing the location and function of the parts comprising it. Following this, the liquid argon dewar assembly is described in detail, outlining all important features. A detailed description of the design of the LAr cell is then presented. We then give a description of how the entire apparatus was assembled and mounted on its stand, and how mechanical vibrations from the cryo-cooler were controlled.

The cleaning procedure of the liquid argon assembly and cell is described, along with the procedure for filling it with liquid argon. The chapter concludes with a discussion on the data acquisition and scintillator triggering systems, with a brief overview of the experimental run procedure.

3.1 The Cryostat

The liquid argon ionization cell and dewar are contained in a cryostat vacuum chamber, see figure 3.1, constructed from a stainless steel cylindrical tube and bellows arrangement, measuring 21.3 cm in outer diameter, and 51.8 cm in length. Welded concentrically to the bottom part of the cryostat was another stainless steel cylindri-

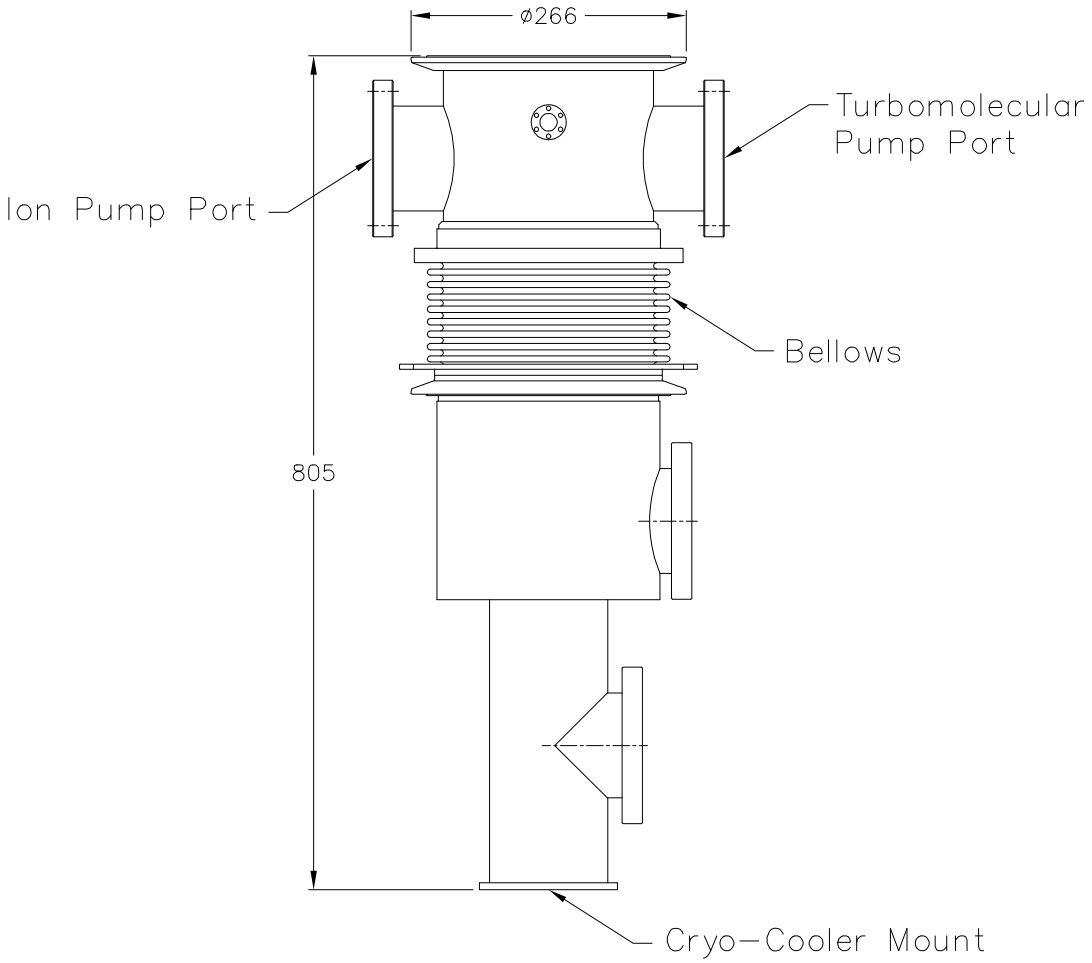

Figure 3.1: Elevation view of the cryostat. All dimensions are in millimeters.

cal tube, of diameter 11.3 cm. The attachment of this tube brings the overall length of the cryostat to 80.5 cm. The top of the cryostat has a machined flange of diameter 26.6 cm which served to seal the vacuum chamber with the lid of the cryostat. Between this flange and the top of the bellows were two vacuum ports: one for a turbo pump for evacuating the chamber, the other for a 60 l/s Varian StarCell ion pump. Also just below this flange was a small vacuum port for attachment of a Penning pressure gauge for monitoring the internal pressure of the cryostat while under vacuum.

The portion of the cryostat bellow the bellows had two access ports. The one just below the bellows allowed access to the heavy copper braid wire that connected the LAr dewar to the cold finger of the cryo-cooler, in addition to allowing the connection of the temperature controller to the copper heat sink on the side of the LAr dewar. The lower of the two access ports remained sealed throughout the entire operation of the apparatus. Finally, at the very bottom of the cryostat arrangement was the cryo-cooler mounting flange.

3.2 Liquid Argon Dewar Assembly

The liquid argon dewar assembly is shown in figure 3.2. The top of the cryostat vacuum chamber was sealed with a mating stainless steel lid using a viton O-ring between the lid and upper flange of the cryostat. Offset from the axis of the lid was welded a preamplifier BNC feedthrough port for the connections between the preamplifiers and the LAr ionization cell. Welded concentrically through the lid was a 5.0 cm diameter stainless steel tube of approximate length 43 cm, which for future reference will be referred to as the neck. The top of the neck was sealed with a conflat flange which housed the two high voltage feedthroughs that provided HV to the cell plates of the liquid argon ionization chamber via two steel wires in the neck. Also on the neck, located just below the HV conflat flange, was a 5.0 cm diameter stainless steel vacuum port for the liquid argon dewar. We refer to this as the pumping and argon entry port. The argon gas that is condensed in the chamber was introduced through this port. To the lower end of the neck the was a 19.4 cm diameter rotatable conflat flange to which the stainless steel liquid argon dewar was bolted. Signal wires ran from vacuum feedthroughs in this conflat flange up along the neck to the underside of the preamplifier BNC feedthrough. The liquid argon dewar is where the ionization

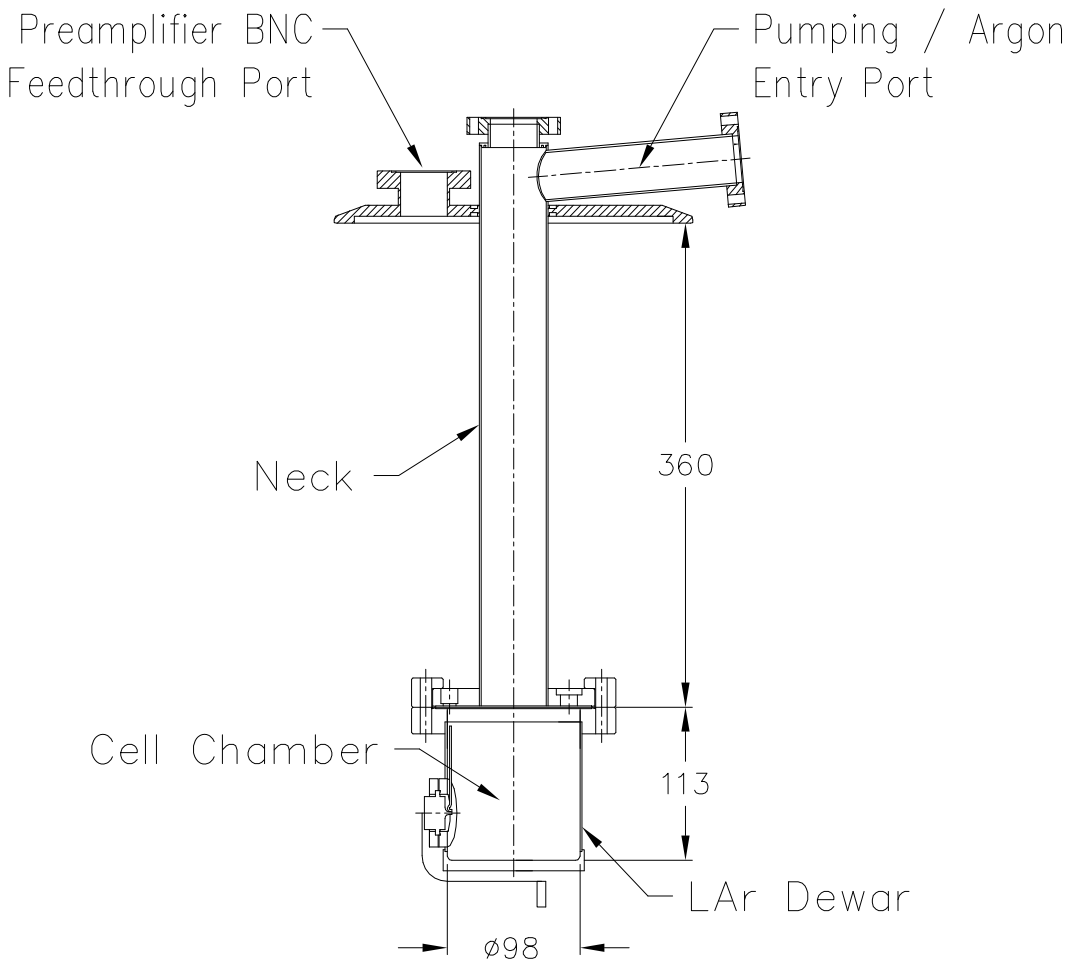

Figure 3.2: Elevation view of the liquid argon dewar assembly. All dimensions are in millimeters.

cell was located. Embedded into the wall of the dewar was a cylindrical slab of copper to act as the heat sink for the cell chamber. A heavy copper braid wire was attached to the exterior side of the copper slab. The copper braid wire provides the thermal contact between the copper slab heat sink and the cold finger of the cryo-cooler.

3.3 The Liquid Argon Ionization Cell

The liquid argon ionization cell was constructed of four square stainless steel plates each of width 62 mm, mounted on four nylon threaded support rods, and stacked in a vertical arrangement above each other, as shown in figure 3.3. The rods were mounted from the flange at the bottom of the neck so that the dewar could be bolted in place onto the flange without disturbing the cell and related wiring. The topmost plate was the HV for the top cell, with the two central plates at ground, and finally the lowest plate of the four provided HV for a second cell. The plate separation for the top cell was 2.0 mm, followed by a 2.0 mm gap separating the two ground plates, and finally a 10.0 mm gap separated the plates of the lower cell. The gaps between the plates were maintained by hollow cylindrical nylon spacers, of appropriate length, inserted over the support rods. The 10.0 mm spacers each had a $\approx$ 1 mm diameter hole drilled in them, and the nylon ready rods had their threads slotted to ensure no air would be trapped anywhere in the system creating virtual vacuum leaks. Finally, the arrangement was held rigidly in place by a set of sixteen double locked nylon nuts tightened from above the topmost plate, and from below the lowest plate.

A length of stainless steel wire was welded to each plate, and in the case of the HV plates, these were connected to the HV feed wires running down through the neck. The signal wires were connected to high vacuum feedthroughs that were welded into the conflat flange of the LAr dewar. From these feedthroughs, single shielded, ungrounded coaxial cables were connected to the preamplifier BNC feedthroughs in the lid of the vacuum chamber. Figure 3.3 shows the cell in its assembled state, situated inside the dewar, in the plan, and in the elevation view, and figure 3.4 shows schematically the wiring scheme for the ionization cell.

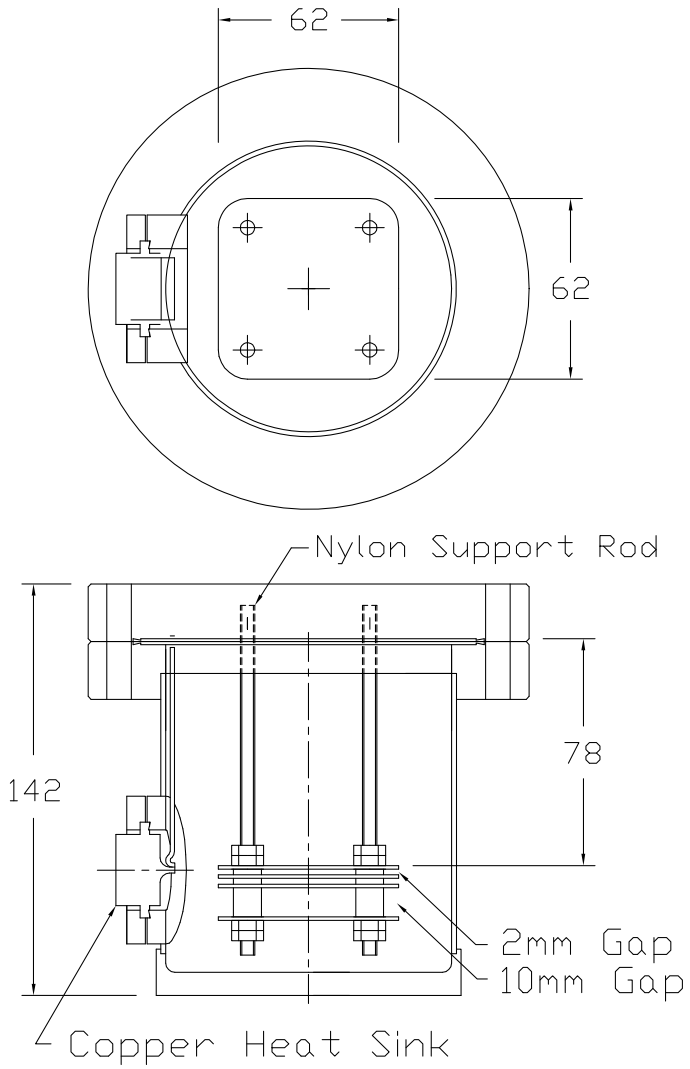

Figure 3.3: The LAr cell, contained in the dewar, as seen from plan view in the upper portion of the figure, and from elevation view in the lower portion of the figure. All dimensions are in millimeters.

The plates and stainless steel wire welded to them were subjected to a cleaning procedure that involved one cleansing with acetone, followed by two cleansings with 95% ethanol. In all steps, the component parts were allowed to air dry before their next cleansing. Following the ethanol cleansings, there was one cleansing in distilled water. Finally, this was followed by a sequence of ten cleansings in deionized water

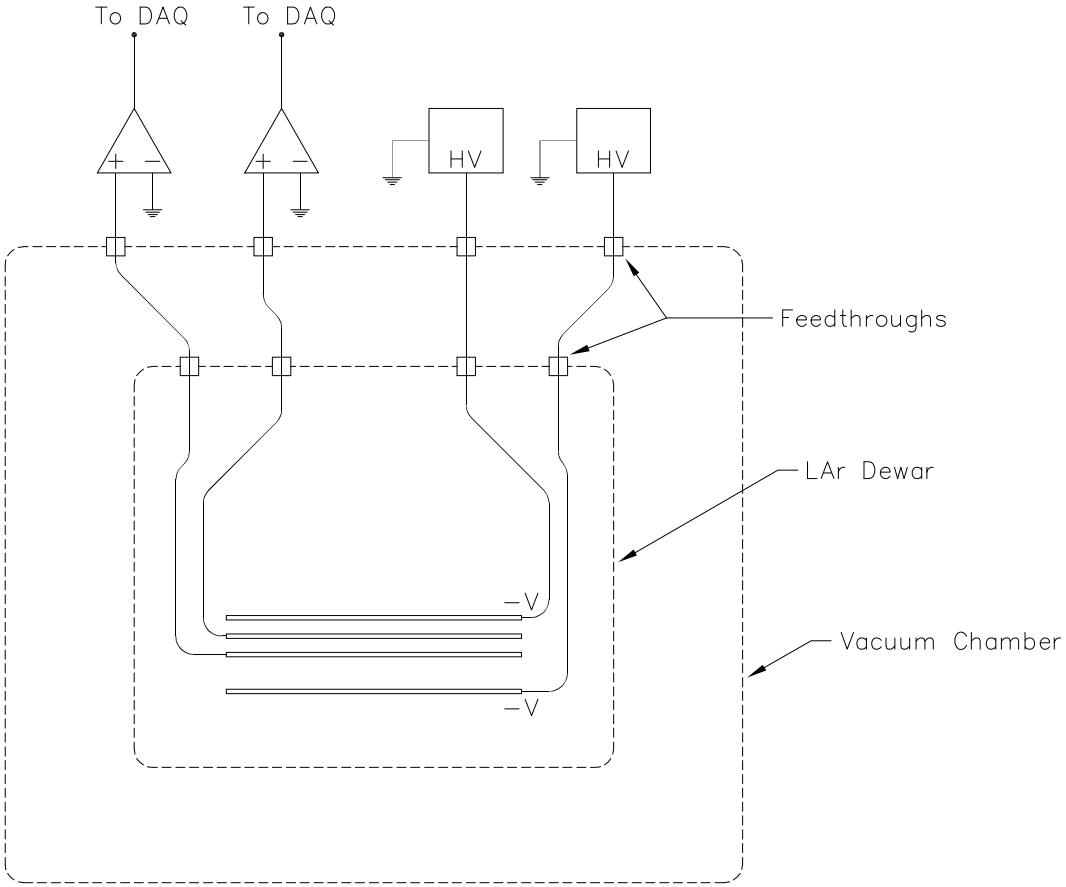

Figure 3.4: Schematic wiring diagram of the LAr ionization cell. Note that relative positions between the objects are not drawn to scale.

having a resistivity of 17.9 MΩ-cm. The nylon components went through the same cleansing procedure, except the acetone cleansing was omitted. Once air dried after the final deionized water rinsing, the parts were assembled into the apparatus to form the cell, and were then subjected to a stream of argon gas to remove any dust or fibres. With the cell cleaned and assembled, and all wiring connected, the dewar was then bolted to the conflat flange at the bottom of the neck sealing the cell with a copper compression gasket.

3.4 Complete Apparatus Assembly

A stand made from 3.89 cm × 3.89 cm box channel steel was constructed to mount and support the cryostat apparatus of figure 3.1. The four legs of the stand measured 90 cm in height and were braced together at the top and bottom by four horizontal cross members connecting each pair of legs. The stand measured 40 cm on each side, and is depicted in figure 3.5. The stand was rigidly bolted into the concrete floor of the lab and the cryostat, with cryo-cooler attached, was supported in the stand by means of a mounting plate attached to the flange just immediately above the bellows. The mounting plate was bolted to the horizontal cross members on the top of the stand.

Approximately half-way between the two access ports on the cryostat, an aluminum disk of outer diameter 28.2 cm was friction clamped to the stainless steel tube that the cryo-cooler was mounted onto. See figure 3.6. Three aluminum pulleys arranged at 120° apart from each other were attached to the disk. A single strand of high tensile strength piano wire was wrapped around each pulley and secured to cross member sections at the base of the stand. The cross members are shown at the bottom of the stand in figure 3.5. The piano wires came under tension due to the collapse of the bellows when the cryostat was evacuated. In this way they served to prevent the bellows from collapsing completely, and also to tie the vibrating cryo-cooler to the base of the stand. During operation of the apparatus, the liquid argon dewar assembly, of figure 3.2 was lowered down into the cryostat of figure 3.1, with the lid sealing the cryostat for eventual vacuum pumping. The heavy copper braid wire was then be connected to the cryo-cooler cold finger, and the temperature controller electronics leads were connected to the copper heat sink on the side of the LAr dewar

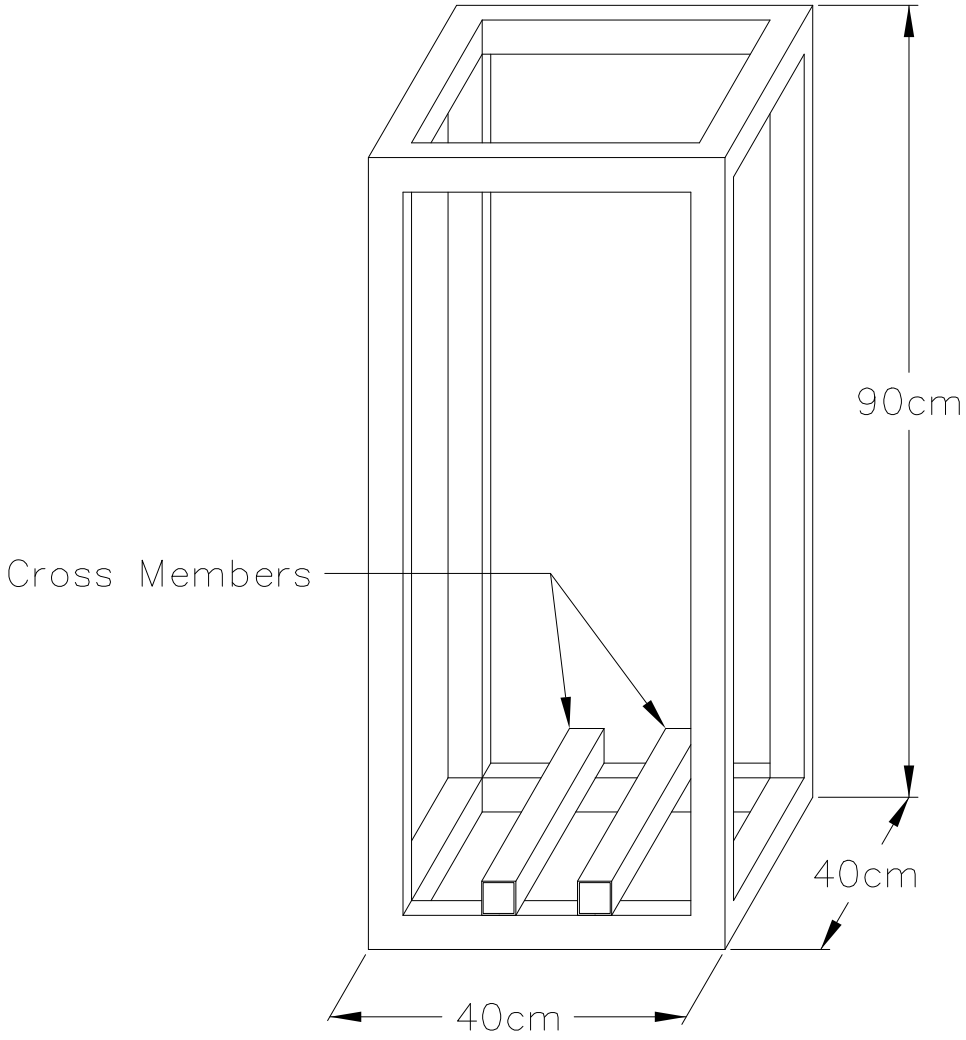

Figure 3.5: The stand.

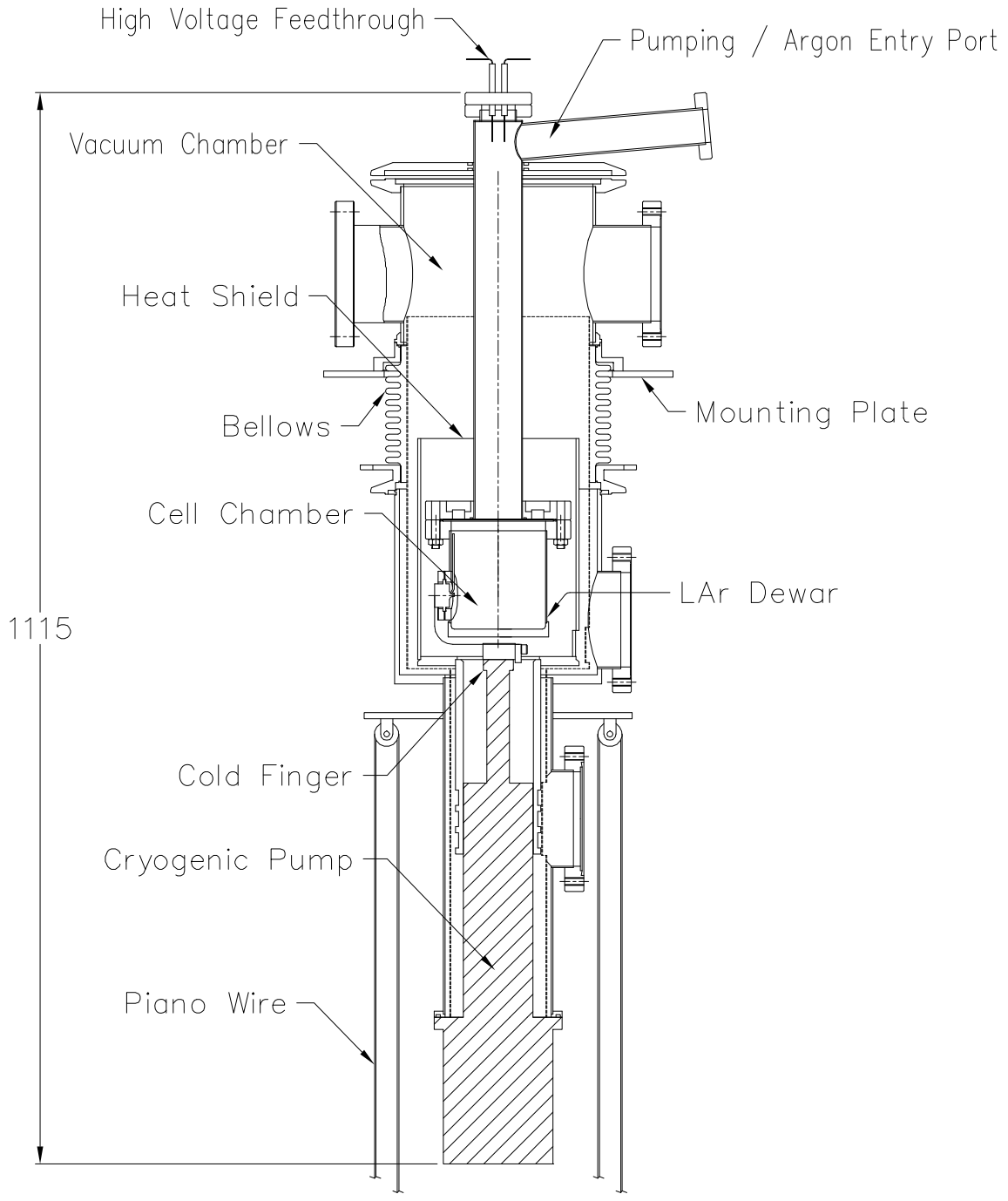

Figure 3.6: The cryostat apparatus as assembled for experimental operation, showing the major components. All dimensions are in millimeters.

in preparation for eventual cryogenic cooling.

The entire experimental arrangement, with the apparatus assembled in its experimental configuration is shown in figure 3.6; note, for clarity the stand is not shown in this figure.

3.4.1 Acoustical Noise Reduction

The cryo-cooler contains a piston expander that generates strong mechanical vibrations. These vibrations manifest themselves as voltage fluctuations on the LAr signal transient. We refer to these fluctuations as acoustical noise. Initial trial runs with the apparatus clearly demonstrated that the acoustical noise originating from mechanical vibrations from the cryo-cooler would make discrimination between signal events and background noise impossible. This section describes the effectiveness of the design and mounting of the apparatus in reducing the effect of these vibrations on the LAr signal transients.

The choice of mounting the cryostat into the stand, using a mounting plate located at the top of the bellows was twofold: this arrangement allowed the bellows to "float" and act as a spring, damping some of the mechanical vibrations coming up from the cryo-cooler, while rigidly fixing the section of the cryostat above the bellows to the stand. It was important to isolate the section of the cryostat above the bellows as much as possible from these vibrations because any vibrations reaching the top section of the cryostat would be transmitted down the neck and into the ionization cell. The piano wire and disk arrangement allowed for some frequency components of the mechanical vibrations to be passed down the wires into the base of the stand. The combination of the cryostat mounting, and the piano wire arrangement, eliminated low frequency baseline voltage fluctuations that were at times on the order of 1 V.

Lower amplitude, higher frequency voltage fluctuations on the LAr signal transients resulted from vibrations of the stand legs. The effect of the vibrations in the stand legs was reduced by stacking two lead bricks each of mass $\approx 14\,\mathrm{kg}$ on each corner of the top of the stand, directly above each leg. The heavy mass over each leg acted to "approximate" having the top ends of the legs rigidly fixed. By connecting a digital oscilloscope, in envelope mode, through a preamplifier to the ionization cell, one could observe the overall envelope of noise coming from the ionization cell from these vibrations. Making fine adjustments in the positions of the lead bricks over each leg, and observing the oscilloscope screen, the acoustic noise envelope coming from the cell was reduced from 65 mV peak to peak down to 30 mV peak to peak.

Additionally, the stand legs were also filled with fine sand to help damp out their translational vibration modes. The effect of this measure was a reduction in the noise envelope an additional 6 mV peak to peak. Lastly, some experimentation was done with the type of signal wire used to connect the cell signal feedthrough of the LAr dewar flange to the BNC connector feedthrough of the preamplifier in the lid of the LAr dewar assembly. It was found that single shielded, ungrounded coaxial cable took the level of acoustical noise down another 3 mV peak to peak, attaining a final acoustic noise envelope of just 21 mV peak to peak. To put these results in perspective: the intrinsic electrical noise envelope from the cell through the preamplifier, with the cryo-cooler switched off, was measured to be 18 mV peak to peak.

Figure 3.7 shows the vast improvement in signal discrimination obtained in having mounted the cryostat apparatus in the way described, and in having made the additional modifications to the stand using the sand, and lead bricks. The transient in the top half of figure 3.7 was acquired prior to mounting the cryostat in the manner

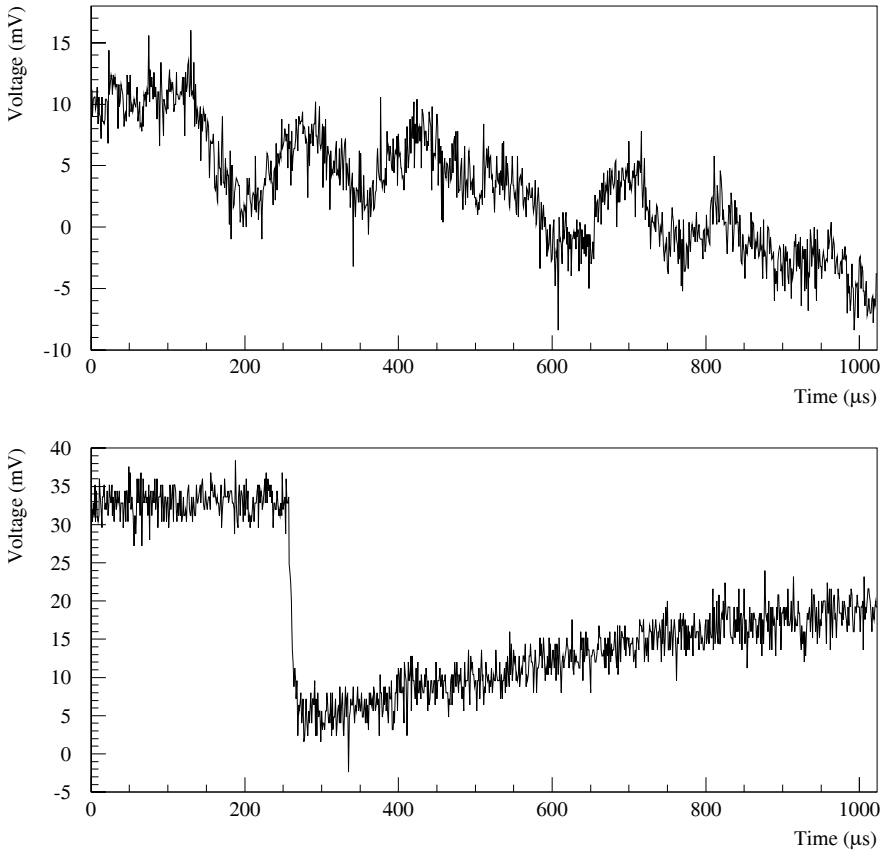

Figure 3.7: The improvement in the acoustic noise characteristics of the cryostat apparatus as a result of mounting it in the stand of figure 3.5, and using the modifications to the stand as described in the text. The upper plot shows a "typical" LAr transient before mounting and modifications were applied, and the lower portion a "typical" transient after modifications were applied.

finally chosen for this work, and is typical of all the transients acquired in that data set; the lower transient was acquired after mounting the cryostat in the way described in the previous sections. Both transients shown were acquired by a digital oscilloscope triggered by a scintillator telescope detector. The transients were acquired with an additional timing filtering amplifier in the acquisition circuit; that is, data that has

been additionally filtered to "remove" acoustical noise. Even with this additional measure, discrimination between data and noise is impossible without the vibration damping modifications, as the top transient in figure 3.7 clearly shows.

These modifications allowed data acquisition using just a preamplifier only, where previously an additional timing filtering amplifier was needed to electronically filter out the acoustic noise. As a result of these modifications, LAr transients from the ionization chamber could be recorded with a wider electronic bandwidth, and with potentially reduced systematic effects from the additional filtering.

3.5 Liquid Argon Filling Procedure

The LAr dewar was evacuated with a turbomolecular pump. Electrical heater coils were wrapped around the dewar, neck, pumping and argon entry port; all the vacuum tubing leading from the pumping and argon entry port to the pump; and the pump itself, to bake all the internal surfaces that would be in contact with argon gas or liquid. Because the mounting rods for the cell were made of nylon, a uniform baking temperature of approximately 70° C was maintained to ensure that the nylon would not warp, or stretch and thus, distort the geometry of the cell. The system was baked and pumped on for a period of approximately five days, attaining an ultimate pressure within the system of 4×10^{-8} mbar. The argon assembly was then removed from the turbo pump.

While the argon dewar was sealed from atmosphere the entire argon assembly was lowered into the cryostat. A heavy copper braid wire running from a copper heat sink on the dewar was attached to the cryo-cooler cold finger, allowing the dewar to be cooled while minimizing the transmission of vibration to the dewar from the cryo-cooler. The cryostat vacuum chamber was then pumped out using the same tur-

bomolecular pump. During this stage of the vacuum chamber pumping, the cryogenic cooler was activated to help bring the internal pressure down faster. When a pressure of 1.1×10^{-6} torr was achieved a StarCell ion pump was also turned on and finally the turbo pump was removed when the pressure in the cryostat reached approximately 7×10^{-7} torr.

The turbo pump was then reattached to the argon system, but the valve to the argon assembly was not yet opened. Heat was then applied to the turbo pump, and all tubing components leading up to the valve that sealed the argon assembly from the pump. This system was then allowed to bake at approximately 120° C for approximately sixteen hours to ensure a thoroughly evacuated system, at which point the heat was turned off and the system was allowed to cool to room temperature. When the ion gauge of the turbo pump indicated a pressure of 1.2×10^{-7} mbar, the valve to the argon system, which had been closed for ≈ 45.5 hr, was opened. No appreciable change in pressure was noted on the ion gauge of the turbo pump, indicating no leaks in the argon assembly. Pumping on the argon assembly then continued for approximately six more hours reaching a pressure at the turbo pump of 6×10^{-9} mbar, at which point the argon assembly was once again closed and isolated from the turbo pump. During this time the cryo-cooler had reduced the temperature of the LAr dewar and cell to 86 K.

Finally, a gettering oven [13] with a titanium charge was attached to a valve connected to the argon assembly. A stainless steel line approximately two inches in length and a bleeder valve with glycerin bubbler, connected the output of the gettering oven to the entry valve. The line was purged to atmosphere, using a flow of gettered argon for approximately 50 minutes. The bleeder valve was then closed, and the entry valve was opened to allow purified argon gas to enter the cold argon

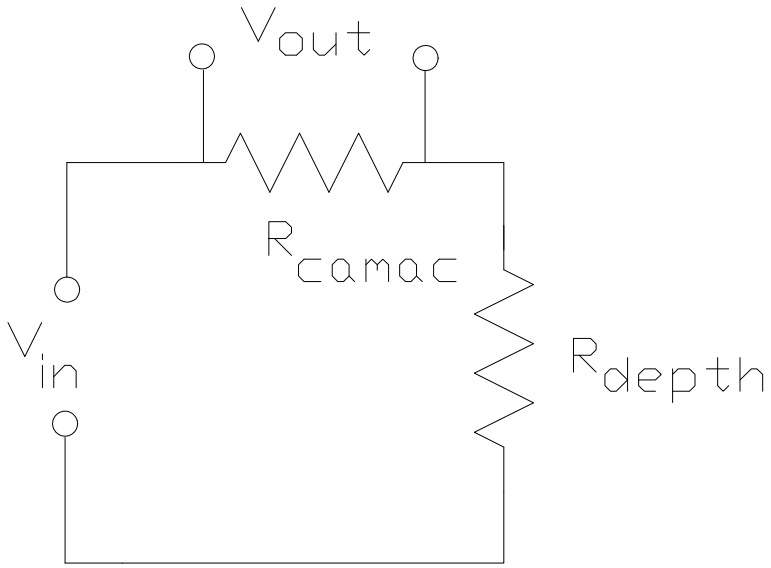

Figure 3.8: Circuit diagram for the depth gage resistor, with $V_{in} = 4.98\,\mathrm{V}$, and V_{out} read by the CAMAC controlled digital voltmeter, and R_{depth} eventually immersed in liquid argon.

dewar. Filling of the argon system, by condensing argon gas in the dewar, then took place over the next 38 hours, monitored by an electronic flow meter, ultimately filling the dewar to a height of approximately 46 mm, ensuring coverage of all four cell plates. A temperature dependent resistor, mounted in the cell chamber 2 mm above the topmost plate, acted as a depth gauge for the height of the liquid argon. An external 96.7Ω resistor was wired in series with the depth resistor, and the voltage of this external resistor was read by a CAMAC controlled digital voltmeter. A total of 4.98 V was applied across this circuit. A schematic representation of the circuit is shown in figure 3.8. A lab bench test using liquid nitrogen indicated that with the depth resistor immersed in LN_2, the voltage should read 2.73 V, with the liquid nitrogen being at a temperature of 77 K. Recall, for the LAr, the temperature was controlled to be at 86 K. Figure 3.9 clearly shows a sharp drop off in the voltage

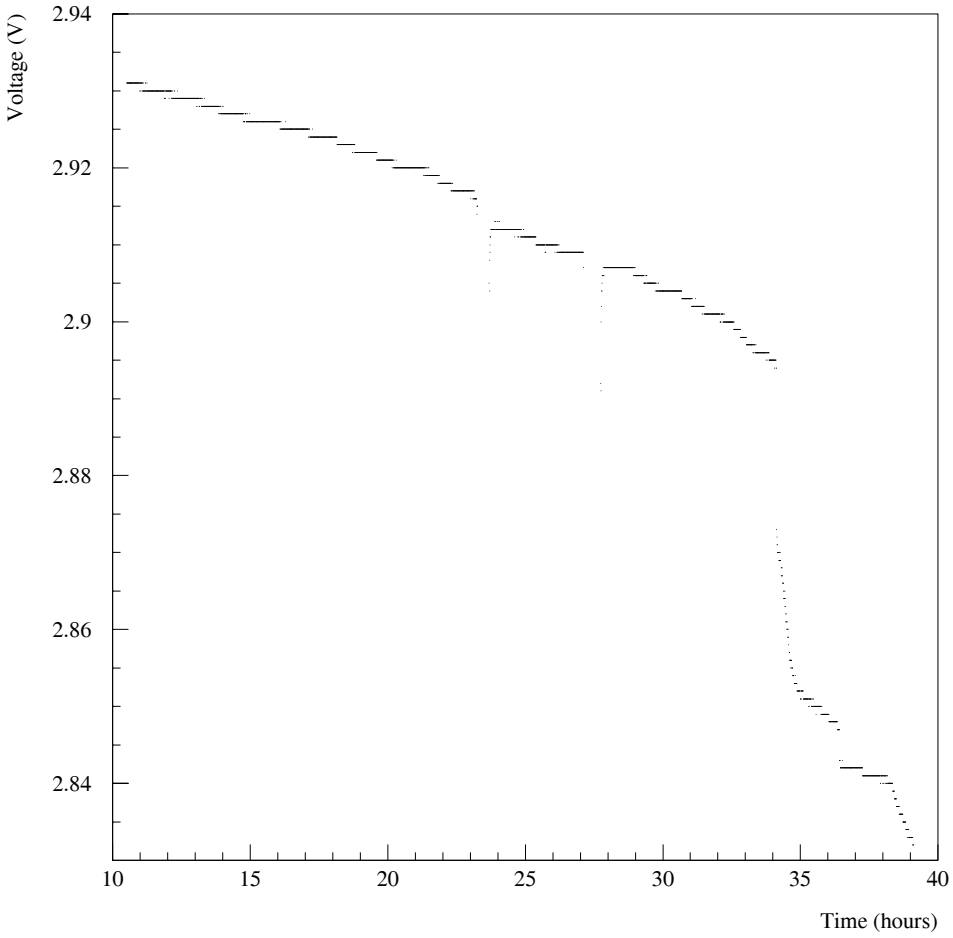

Figure 3.9: Voltage from external 96.7Ω resistor versus run time of the argon entry. Notice the sharp drop off in the voltage at 34 hours, indicating the internal depth resistor immersing the in the liquid argon. The quantized appearance of the data is a result of the digitization of the CAMAC analog to digital converter.

around the 34 hour mark, indicating initial immersion in the liquid argon took place at this time. The last reading of the depth resistor before closing off the argon entry valve was 2.83 V. These numbers indicate that the depth resistor was immersed in the liquid argon by the 40 hour mark.

3.6 Data Acquisition System

High voltage to the cell was supplied by a Bertran 380P power supply filtered by a Butterworth low pass filter of 50 ms time constant [17]. The purpose of the filter was to smooth out any high frequency voltage fluctuations from the HV source, thus producing a constant HV on the cell and thereby eliminating induced signals from HV induced charge effects.

Voltage transients acquired from the LAr cell were first passed through a spectroscopic charge integrating preamplifier[1] connected via a BNC high vacuum feedthrough in the lid of the cryostat to the signal wire of the ground plate, as shown schematically in figure 3.4. From the preamplifier, the transient signals were observed with a digital oscilloscope[2], AC coupled to the preamplifier. The analog voltage transient was converted into digital format and saved to disk on a 386 microprocessor computer. Figure 3.10 shows schematically the set up of the data acquisition electronics.

Low frequency variations in the zero voltage baseline caused by remaining undamped mechanical vibrations from the cryogenic pump required that the oscilloscope be set to an external triggering mode for acquiring LAr transients. The trigger was comprised of a scintillator telescope consisting of two scintillator paddles, 10 cm $\times$ 10 cm $\times$ 0.64 cm in size, separated by a vertical distance of 138 cm. The signals from the two scintillators were set to be in coincidence for cosmic rays traversing both scintillators by stacking the paddles directly on top of each other and adjusting the timing of the electronics. After separating the scintillators by 138 cm, a 5 ns delay time of the top scintillator was imposed, to correct for the average time of flight of the

[1] Tennelec TC 170

[2] Tektronix 2440

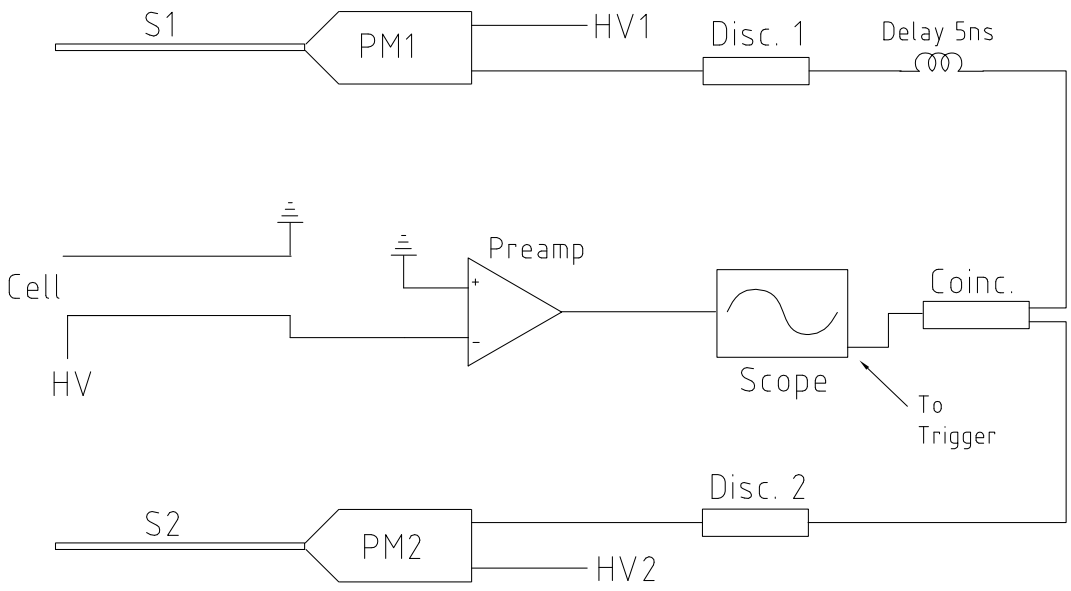

Figure 3.10: Schematic diagram showing the major components of the data acquisition electronics. The abbreviations are as follows: PM = photomultiplier: S1,S2 = scintillator 1 and scintillator 2: Coinc. = coincidence module: Disc. = discriminator module.

hard component of cosmic rays. Both photomultipliers were set to 1850 V determined from efficiency plateau curves for each. The output pulses of the photomultiplier from each scintillator were passed through a pulse height discriminator. Observation of the photomultiplier pulses on the digital oscilloscope indicated that a setting of -100 mV on the discriminator would ensure an adequate cut off of random noise as indicated by the efficiency plateau measurements. The resulting NIM pulses from the discriminator module were then sent through respective delay boxes to ensure a relative 5 ns delay time between the NIM pulses, and then finally into a coincidence module. See figure 3.10. The NIM pulse pairs in coincidence triggered the coincidence module to send a NIM pulse to the trigger of the scope causing it to save to disk the contents of its buffer.

The expected count rate of cosmic ray muons passing through the ionization cell

was calculated based on the known cosmic ray muon rate and the geometry of the scintillator trigger. The solid angle, $d\Omega$, subtended by a planar region lying in the $x-y$ plane, seen by an arbitrary point $P(x_p, y_p, z_p)$, is given by [14],

$$d\Omega = \sum_{i=1}^{2}\sum_{j=1}^{2} \delta_{ij} \arctan\left(\frac{(x_i - x_p)(y_j - y_p)}{z_p\sqrt{(x_i - x_p)^2 + (y_j - y_p)^2 + z_p^2}}\right) \quad , \tag{3.1}$$

with

$$\delta_{ij} = \begin{cases} 1\,, & i = j \\ -1\,, & i \neq j \end{cases}$$

and where x_i and y_i, for $i = 1, 2$, are the bounding coordinates defining the planar region. Figure 3.11 shows the defining geometry for equation 3.1. As stated in §2.3, the total cosmic ray intensity at sea level is $90\,\mathrm{m^{-2}s^{-1}sterad^{-1}}$. Integrating equation 3.1 over the surface of the top scintillator of the telescope, with the bottom scintillator playing the role of the planar region, represented by rectangle $ABCD$, and multiplying the result by the intensity gives an hourly cosmic ray triggering rate of approximately $17\,\mathrm{hr^{-1}}$, with approximately $6.5\,\mathrm{hr^{-1}}$ passing through both scintillators and the LAr cell; a geometrical acceptance efficiency of 36%. The experimental count rate observed was $25\,\mathrm{hr^{-1}}$. Statistically, the measured and expected values are consistent with each other, but it was also discovered that the scintillators themselves have a high random count rate associated with them. When taken completely out of coincidence with each other, and allowed to operate for 1000 s on two separate trials; trial one yielded a random count rate of approximately $8\,\mathrm{hr^{-1}}$, and trial two yielded a count rate of approximately $3\,\mathrm{hr^{-1}}$.

The singles count rate for each scintillator used were both approximately 5 Hz. The timing resolution of the coincidence module is 3.5 ns and the pulse widths were set at $30/, /mboxns$. With these values, a true random rate of $\approx 3 \times 10^{-4}\,\mathrm{hr^{-1}}$ should

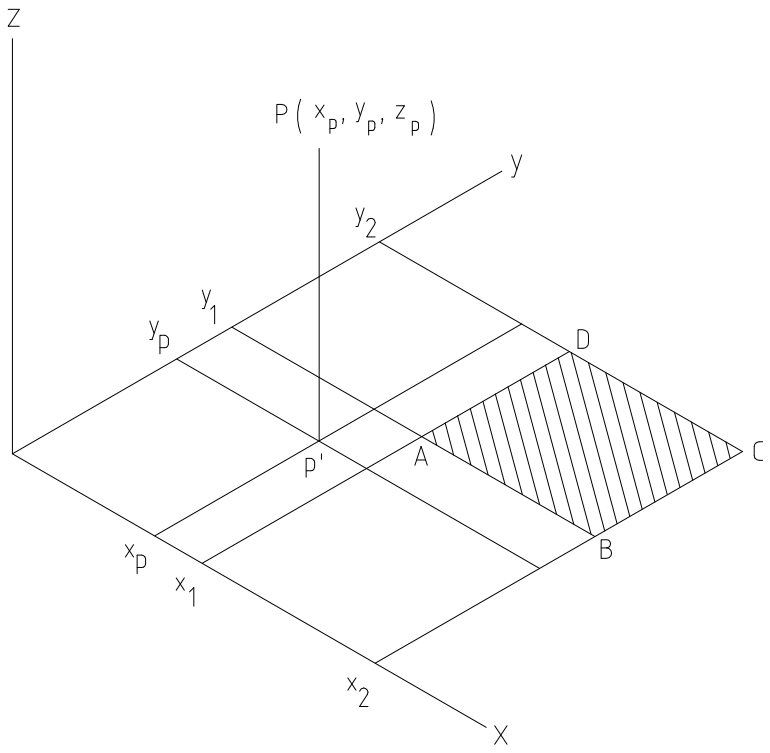

Figure 3.11: The geometry in which equation 3.1 applies. The hatched rectangular region, ABCD, defines the solid angle, $d\Omega$, with respect to the point $P(x_p, y_p, z_p)$.

be expected. The discrepancy in the experimental and predicted rates cannot be explained by way of true random coincidences. Broadcast noise, or some other form of electrical interference is one possible explanation for the unusually high random count rates observed. This extra count rate will have no effect on the analysis: it simply translates into a higher number of data files consisting purely of electrical noise; that is, false events.

The experiment ran continuously over a period of thirty-four days. Data was taken from both cells, with data from the 10.0 mm gap cell taken at electric field settings of 3 kV/cm, 1 kV/cm, and 500 V/cm. Data from the 2.0 mm gap cell was taken at 3 kV/cm only. A total of 4876 triggered events were collected for this study. Comprising these events were: 1148 events at 3 kV/cm, 1008 events at 1 kV/cm, 1130 at 500 V/cm all on the 10.0 mm gap cell, and 1590 at 3 kV/cm on the 2.0 mm gap cell, making a total of four data sets.

Chapter 4

Data Analysis

The analysis of the LAr transient waveforms produced by cosmic ray interactions in the liquid argon ionization chamber are discussed in this chapter. The first part of this chapter discusses the impulse response of the electronics chain. The data is presented and a fit of the measured impulse response is made to the impulse response model presented in chapter 2. We then discuss the development, usage, and optimization of a digital filtering technique for discriminating signal events from background events. The optimization of the filter is presented.

The fourth section of this chapter discusses the selection cuts and criteria imposed on the data for eventual analysis. Finally, the chapter concludes with a detailed discussion on the procedure used for eventual determination of the free electron lifetime.

4.1 Impulse Response of the Preamplifiers

Two preamplifiers were used in this experiment for acquiring data from the LAr cell; namely, an amplifier for the 10.0 mm gap cell, and one for the 2.0 mm gap cell. These amplifiers were not interchanged between the two cells at any time throughout the experiment. As a matter of convention, future reference to the phrase "impulse response" will refer to both sets of data acquired from the 10.0 mm gap cell and

2.0 mm gap cell, unless otherwise stated.

Impulse data was generated by injecting a step voltage input (rise time $\approx$ 8ns) into the high voltage input of each of the LAr cells, and acquiring the output signal through the electronics chain of the experiment. See figure 3.10 as reference on the electronics chain. The LAr cell is a parallel plate capacitor, with the 2.0 mm gap cell having a measured capacitance of 60 pF, and the 10.0 mm gap cell having a measured capacitance of 20 pF. Therefore, the step voltage input, $U(t)$ is differentiated to a delta function[1] current pulse. We then have for the current, $i(t)$,

$$i(t) = C\frac{dV}{dt}\,,$$

where C is the capacitance and,

$$\frac{dV}{dt} = \frac{dU}{dt} = \delta(t)\,,$$

where

$$U(t) = \begin{cases} 1\,, & t \geq 0 \\ 0\,, & t < 0\,, \end{cases}$$

and $U(t)$ normalized to arbitrary voltage units[2].

The electronics chain impulse response function given by equation 2.15 has two time constants, τ_1 and τ_2, the integration time and differentiation time, respectively, associated with each preamplifier that require determination. We do not consider the characteristic time constant of the oscilloscope here, as it was absorbed into an overall normalization constant. For both preamplifiers, a total of 1000 impulse

[1]Strictly speaking, this is only true in the sense where one defines $\delta(t)$ and $U(t)$ in terms of limiting sequences. See Arfken, *Mathematical Methods for Physicists*, Academic Press, Inc. 1985, pg. 490. Also see [11].

[2]The mathematical theory is equivalent whether $U(t)$ has been normalized to unity, or is arbitrary in value.

transients were recorded for each preamplifier: 500 recorded with a total time duration of 2.046 μs, and 500 with a total time duration of 2046 μs. The short time duration allows the integration time of the preamplifier to be resolved, while the long time duration allows the differentiation time of the preamplifier to be extracted. From each set of 500 files, an ensemble averaged impulse response was generated and figures 4.1 and 4.2 show the these ensemble averaged impulse response data for the two preamplifiers, along with the associated fits to the data. As the short time scale and long time duration data are different measurements of the same phenomenon, simultaneous fitting of formula 2.15 using MINUIT [15] on both the short and long time duration data was performed for each preamplifier. It can be clearly seen in the top portions of figures 4.1 and 4.2, that both preamplifiers exhibit a deviation from model behavior on the short time duration, with the preamplifier for the 10.0 mm gap cell suffering from high frequency ringing. Various attempts to improve the model, treating the oscilloscope as an RC-integrator only, or RC-differentiator only, were not successful. The model given here is the most simple, while giving the best fit. The resulting uncertainty in the electronics model will be incorporated into the systematic errors.

A satisfactory fit for the 10.0 mm gap impulse data proved to be problematic, given the nonideal behavior of its response on the short time duration data. Trying to include all data points from the 2.046 μs time duration data gave unsatisfactory fits, with the "edge" on the integration time for the short time duration data not being steep enough. The reason for this appeared to be due to the elevated tail seen on the short time duration data, as seen in the top half of figure 4.1. Effectively, an integration time constant could not be found that could represent the sharp integration time, and simultaneously, round out quickly enough to be able to fit a line

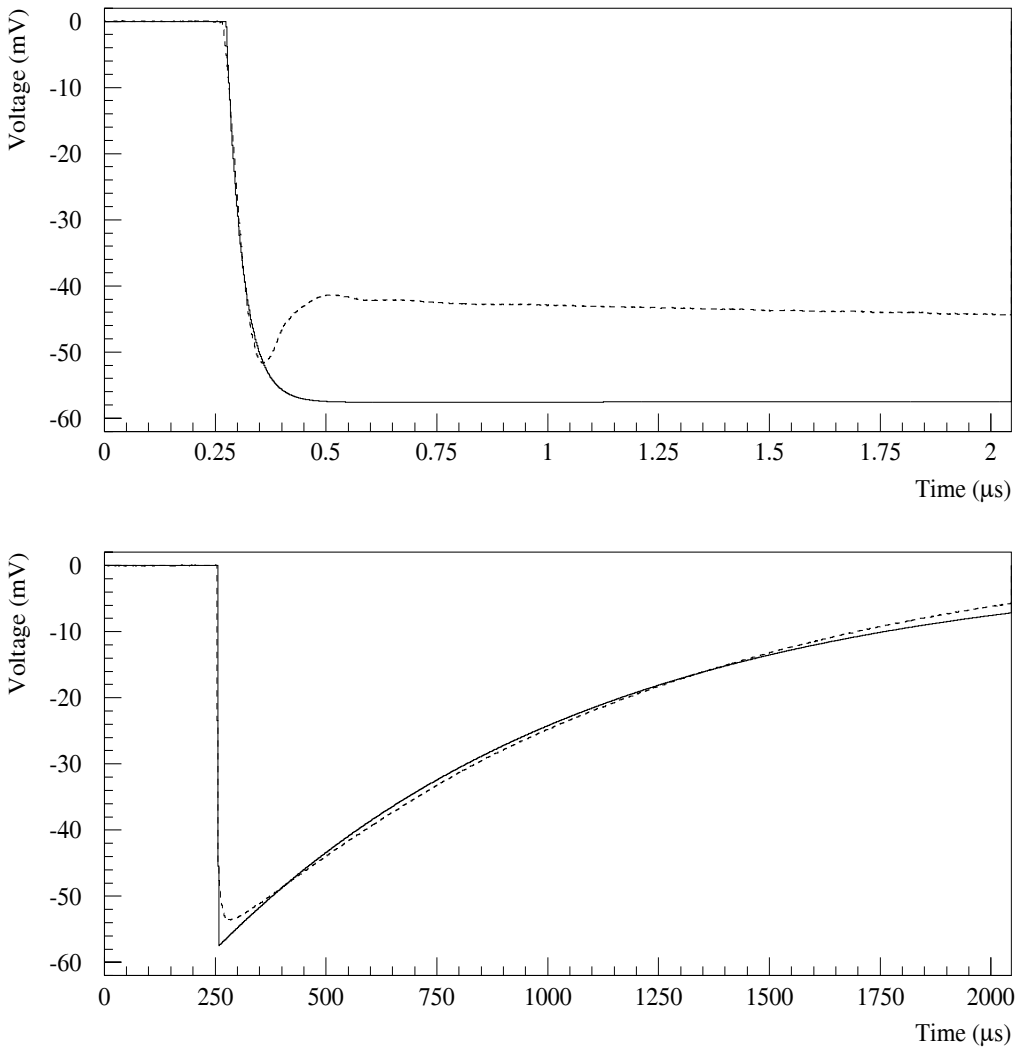

Figure 4.1: Measured ensemble averaged impulse response (dashed line) for the 10.0 mm gap LAr cell, shown with fit (solid line).

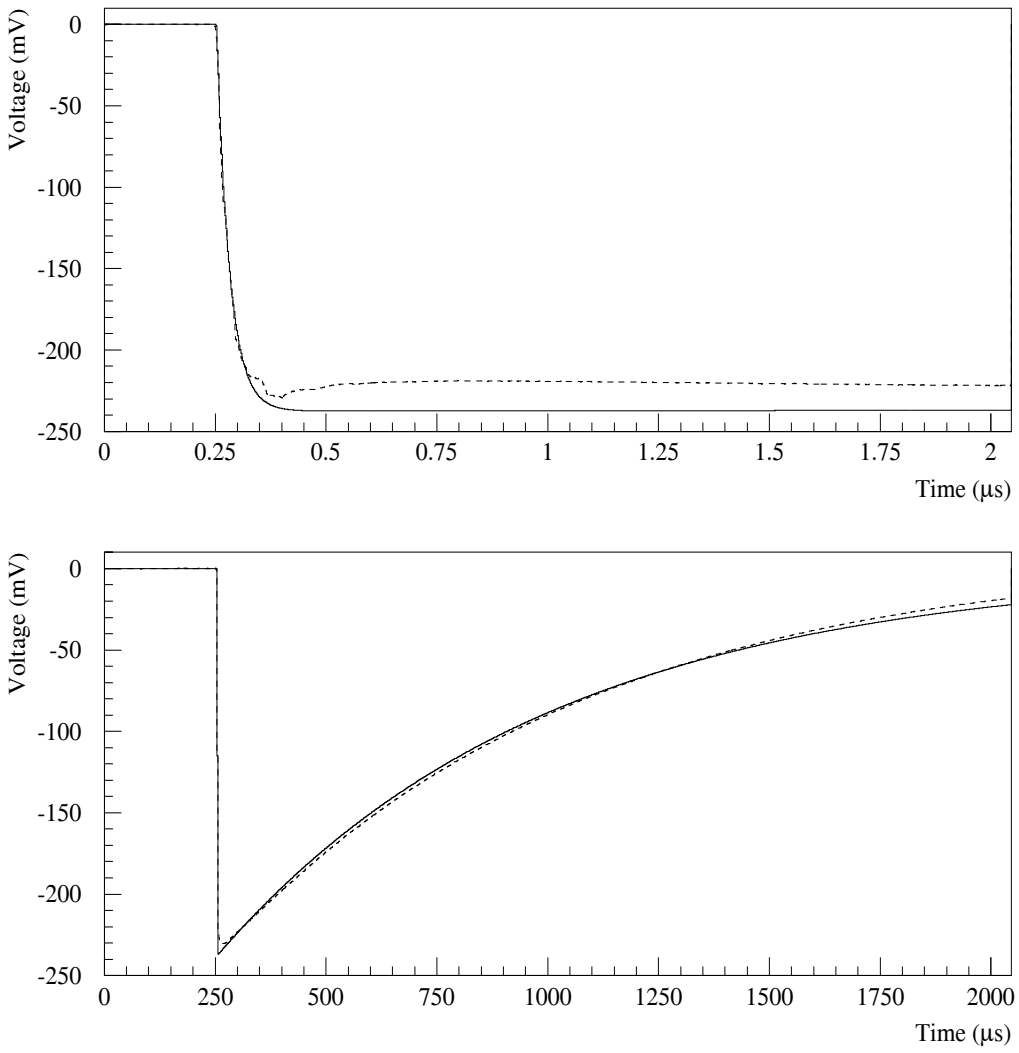

Figure 4.2: Measured ensemble averaged impulse response (dashed line) for the 2.0 mm gap LAr cell, shown with fit (solid line).

Preamplifier	τ_1 (μs)	τ_2 (μs)
10.0 mm gap	$(3.70 \pm 0.05) \times 10^{-2}$	$(0.858 \pm 0.002) \times 10^{3}$
2.0 mm gap	$(2.95 \pm 0.01) \times 10^{-2}$	$(0.7547 \pm 0.0001) \times 10^{3}$

Table 4.1: Summary of impulse response time constant parameters for both preamplifiers used for the LAr experiment.

Preamplifier	t_0 (DL) (short)	t_0 (DP) (long)
10.0 mm gap	(137.7 ± 0.2)	$(128.97 \pm .002)$
2.0 mm gap	(127.0 ± 1.0)	(127.99 ± 0.002)

Table 4.2: Summary of the impulse response trigger point parameters for both preamplifiers used for the LAr experiment, where "short" refers to the 2.046 μs time duration data, and "long" refers to the 2046 μs time duration data. The trigger positions are quoted in terms of their digitization point (DP). These can be converted into time values by multiplying by 2×10^{-3} μs.

through the elevated tail in the upper portion of figure 4.1. Because fitting the integration time accurately is important to reduce any correlations with the electron lifetime, only the first 178 data points, or 0.356 μs, of the short time duration data were included in the global fit of the 10.0 mm gap impulse data. As can be seen from the top portion of figure 4.1, the fit of the integration time is satisfactory with this condition imposed.

The fits of the 2.0 mm gap data seen in figure 4.2 were performed using all data points. We can see that the fit performs well on the integration time, but again is unable to round over fast enough to fit a line through the tail on the short time duration data. Here again, the tail of the fit falls below the tail of the data. The tail in these data is not as elevated as in the 10.0 mm gap data; and thus, the fitting routine was able to find a time constant that satisfactorily fits the integration time, while doing its best to accommodate the elevated tail in the upper portion of figure

4.2. Note that the time constants determined for both preamplifiers are of the same order of magnitude, as expected, and the general qualitative features of the fits are the same, even though the fitting methods for each preamplifier differed in the total number of data points used.

Finally, the triggering points of each data file, with exception of the long time duration data of the 10.0 mm gap cell were also allowed to float in the fits to give the fitting routine a few more degrees of freedom to optimize the fits with. We see that the trigger position of the short time duration data for the 10.0 mm gap data is almost 10 ADC counts higher than what it should ideally be at; namely 128. The fits are still accepted with this value for the trigger point on the basis that the LAr transient data was taken on a time duration setting 10 times longer than the short time duration data of the impulse response. In short, the "jump" in trigger position obtained by the fit to the upper curve in figure 4.1 is just under one ADC count on the LAr transient data time duration, and so, would not be within the resolving power of the oscilloscope during LAr transient data acquisition. The results of the fits are summarized in tables 4.1 and 4.2.

4.2 Digital Filter Development

The digitized LAr transient pulses have 1023 time samplings in each. Further processing of the digitized pulses can be done using digital filtering. Essentially, a digital filter is a convolution of the sampled data points with a vector of weights, as equation 4.1 shows,

$$y_n(t) = \sum_{k=-\infty}^{\infty} c_k u_{n-k}(t). \tag{4.1}$$

where y_n is the filter output, c_k is the weighting term, and u_n is the nth input value.

The general theory of digital filters is covered in Appendix A. The sampling rate of the oscilloscope for all LAr transient data sets in this analysis was 50 MHz. The resulting Nyquist frequency on which the digital filter is to be constructed is then half of the sampling frequency, namely 25 MHz. The filter was constructed from a Fourier series expansion of a unit function, $\lambda(f)$, on the frequency interval $[3.0, 8.0] \times 10^2$ kHz, described by,

$$\lambda(f) = \begin{cases} 0\,, & 0 \leq f < 3 \times 10^2 \\ 1\,, & 3 \times 10^2 \leq f \leq 8 \times 10^2 \\ 0\,, & 8 \times 10^2 < f < 25 \times 10^3\,, \end{cases} \tag{4.2}$$

where it is understood the values shown in equation 4.2 are in units of kHz. Figure 4.3 shows the result of a 86 term Fourier series expansion of the unit function. The top portion of the figure shows the unit function, the standard 86 term Fourier series representation of the filter, and the Lanczos smoothed version of the standard 86 term series, on a linear plot. The lower portion shows the same plots as just described, only on a log-linear plot. The filter smoothed with Lanczos smoothing factors, clearly reduces undesirable ripples caused by the truncation of the Fourier series (see Appendix A). The smoothed version of the filter was used for this analysis.

Points at the beginning and end of the waveform are used to initialize and terminate the filtering sequence. In the case of the 86 term filter, from equation A.2 with $N = 85$, the first data value that can be used in the initialization is the 85th point. In the pretrigger region of the pulses, there are 128 channels. With the initialization required to begin at the 85th data channel the 86 term filter will, in the end, produce only 43 points in the pretrigger region of the filtered pulse. Figure 4.4 shows how the filter acts on a theoretical 3 kV LAr transient. As can be clearly seen, the pretrigger region of the filtered pulse is not horizontal, and so, cannot be used for an appropriate baseline shift for obtaining the absolute pulse heights of the filtered transients. For

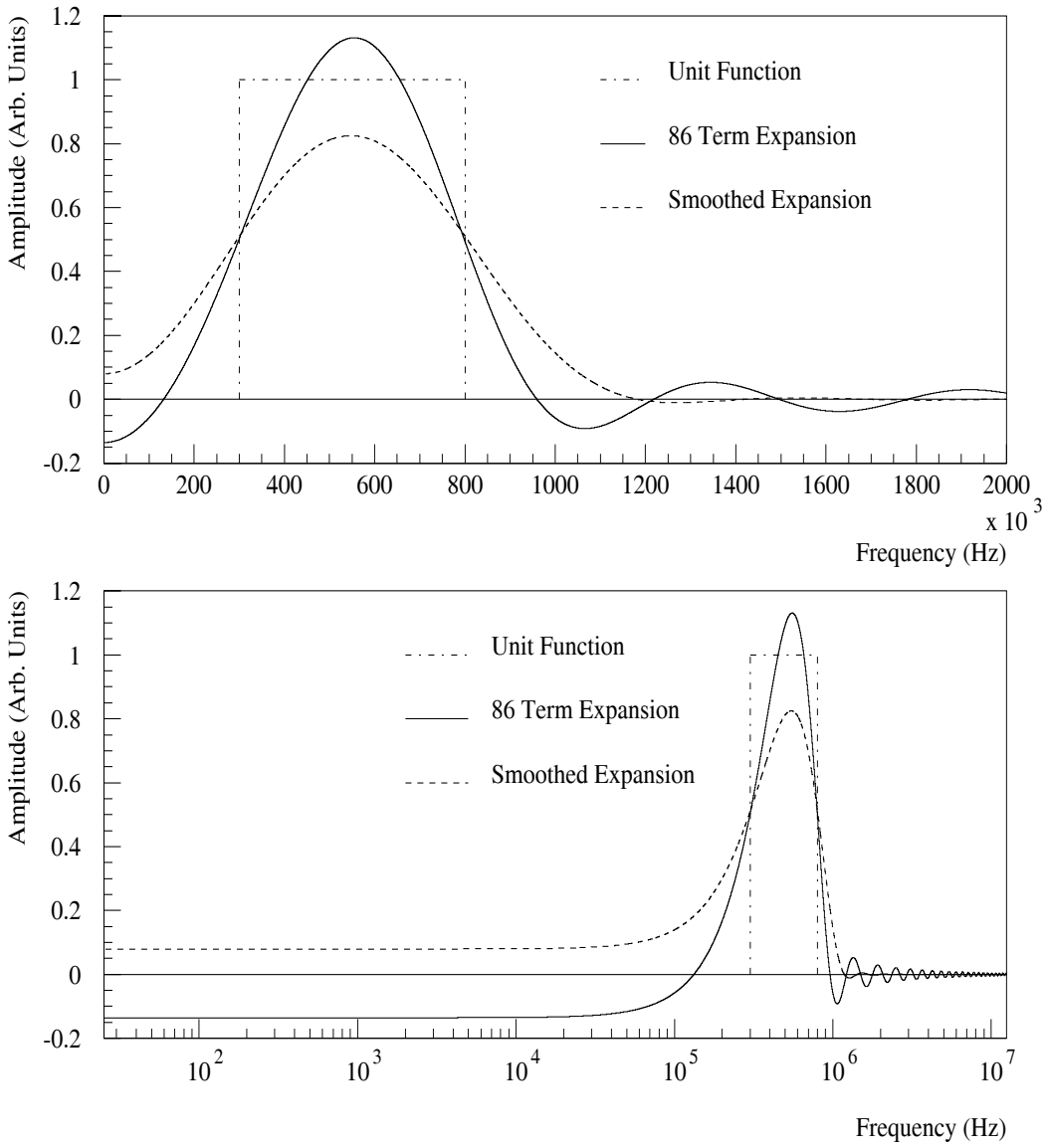

Figure 4.3: Fourier series frequency space representation of the band pass filter used to analyze the LAr transient pulses, shown on a linear scale in the upper half and log-linear in the lower half of the figure. The solid line shows the 86 term Fourier series representation and the dashed line shows the Lanczos smoothed representation of the same filter. The unit height function is shown as reference.

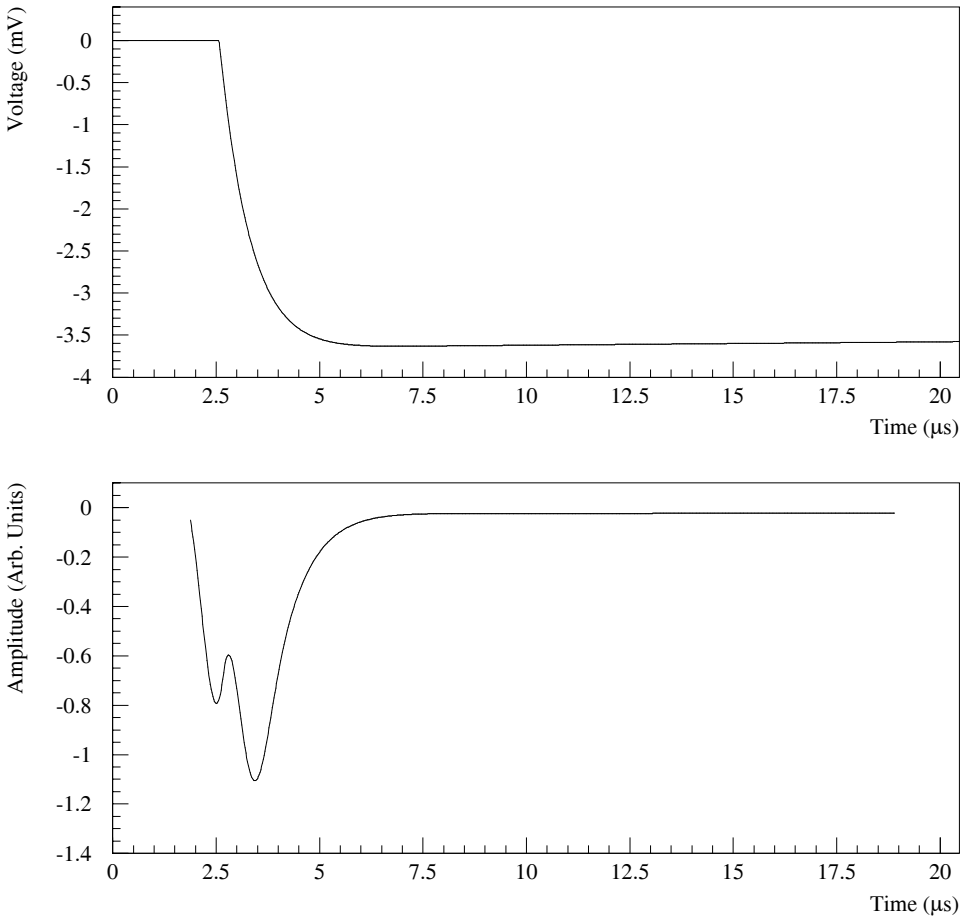

Figure 4.4: A theoretical LAr transient in the top portion of the figure, and its corresponding digitally filtered pulse shown in the lower portion. Notice the absence of data in the leading and tailing regions of the filtered pulse due to initialization and termination of the filtering convolution.

this reason, baseline shifts of the filtered pulses were performed by computing the average value, $\langle V \rangle$, of the pretrigger region of each original LAr transient. Mathematically, a baseline shift in the original LAr transient would amount to subtracting off of each digitized voltage value the amount $\langle V \rangle$; that is,

$$u_n \mapsto u_n - \langle V \rangle,$$

so that all voltage values in the pulse would be with respect to zero voltage. Substituting these baseline shifted input values into equation A.2 will produce as the output,

$$y_n = c_0(u_n - \langle V \rangle) + \sum_{k=1}^{N=85} c_k(u_{n-k} - u_{n+k}) \,. \tag{4.3}$$

It can be seen, comparing this result to equation A.2, that the only difference between this new output and what we would have had originally, without a baseline shift, is the term $-c_0\langle V \rangle$. This new term represents the effect a baseline shift from the original LAr transients would have on the filtered transients. Thus, subtracting $c_0\langle V \rangle$ from each filtered LAr transient will produce a filtered transient that has voltage values with respect to zero voltage.

4.3 Filter Optimization

As shown in equation 4.2, a bandpass filter of width 500 kHz, centered at a frequency of 550 kHz was used. The width of this band pass was chosen so as to minimize its width on the Nyquist interval, while also being able to approximate the unit function with a truncated Fourier series using a reasonably small number of terms. The centring of the bandpass filter around 550 kHz was determined by calculating the signal to noise ratio as a function of the filter's central band frequency for the four data sets and maximizing the ratio.

The transients were screened to remove pulses that saturated or fluctuated into an inverted signal. The details of the selection is described in the next section of this chapter. The transients that passed these selection cuts were combined to make an ensemble averaged transient for each data set. The data sets were then subjected to digital filtering with a bandpass filter of width 500 kHz. The location of the central band frequency of the filter was incremented in 100 kHz steps. For each central band frequency, the filtered pulse height was recorded for each ensemble averaged LAr transient. The pulse height, see figure 4.4, was taken as the minimum value of the transient after processing through the digital filter. These pulse heights are taken as the signal amplitude.

To determine the level of noise passing through the filter, a set of transients where the muon missed the ionization cell were selected for each HV setting of the cell. The transients in each of these sets that had their minimum filtered digitization level occurring beyond 6 μs, that is well beyond the time the signal should have peaked at, as again seen in figure 4.4, were taken as noise transients. These were used to generate an ensemble averaged root mean square noise level, σ, for each data set. The "level" of noise passed by the filter depends on the width and central band frequency of the band pass used. The "level" of noise can be characterized by the root mean square of equation B.5; that is,

$$\text{RMS Noise} = \sigma \sqrt{\sum_{k=-N}^{N} c_k^2}\,, \tag{4.4}$$

where c_k is the kth filter coefficient. To prevent biasing the level of noise, the number of noise files used for each ensemble RMS was required to be equal to the number of files that went into generating each data set's averaged LAr transient. This procedure is exactly equivalent to filtering each noise pulse individually, and then taking these

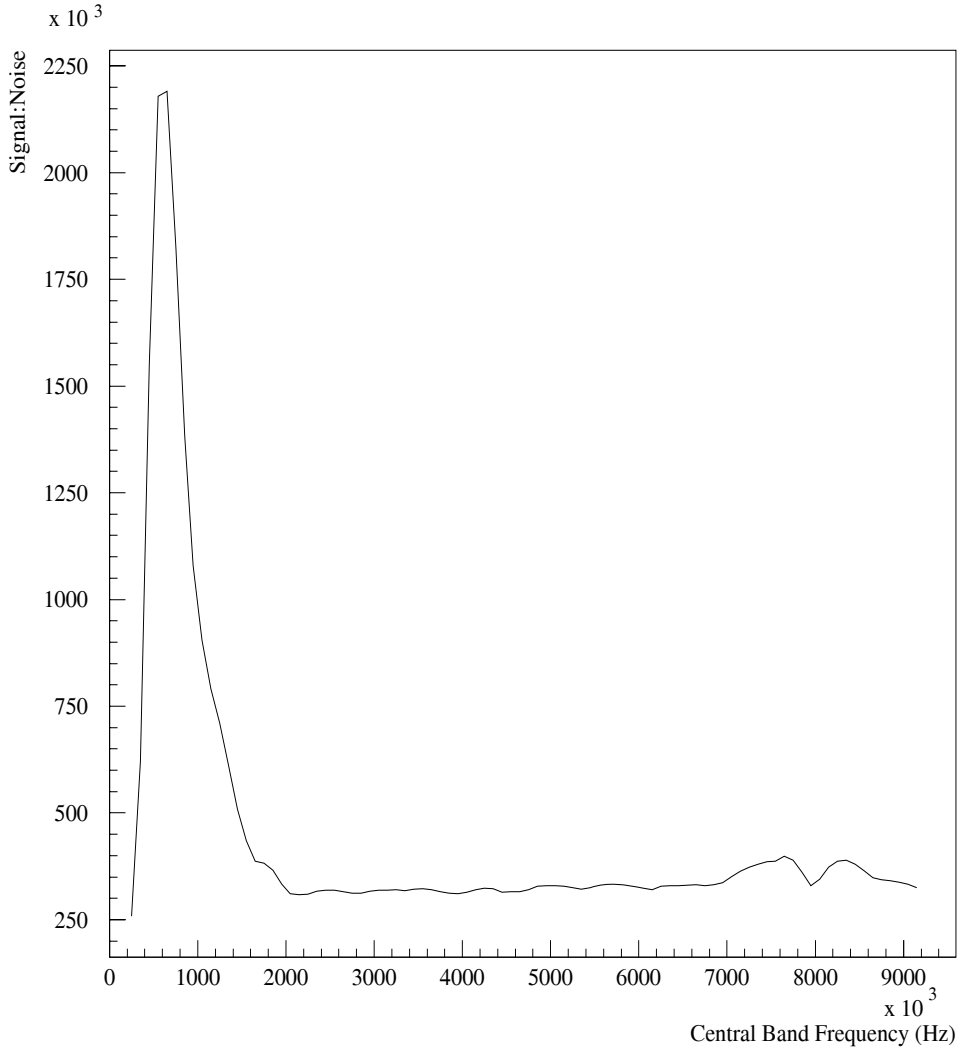

Figure 4.5: Signal to noise plot as a function of central band frequency of the digital filter for the 3 kV/cm, 10.0 mm gap data set.

individual noise values to generate an overall arithmetic average from them for each data set, because the algorithm for digital filtering is linear. Doing the ensemble average noise transient first, and then using equation 4.4 saves computing time.

The signal to noise ratio then, is defined as the ratio of the minimum pulse height

of the averaged LAr transient output of the filter to the ensemble average RMS noise, for each central band frequency. A sample plot of the signal to noise ratio as a function of the central band pass frequency is shown in figure 4.5 for the 3 kV/cm, 10.0 mm gap data set. The plots for the other three data sets looked very much the same as figure 4.5. The optimum central frequency is clearly indicated by the strong peak in the plot of the ratio, occurring at 550 kHz.

4.4 Selection Criteria

The measurement of the electron lifetime for was obtained by producing the ensemble averaged LAr transients from the data for each applied electric field. To select the individual LAr transients, used in the averages, the data was required to pass three selection criteria in order to prevent the contribution of saturated pulses, false events, and inverted pulses to the ensemble averages.

The first cut imposed on the data involved selecting only those pulses that did not exceed the dynamic range of digitization of the oscilloscope; i.e. the elimination of the saturated pulses. This was done with each pulse by ensuring that all of the digitized values in the transient fell within the dynamic range of ± 123 ADC counts. If an individual transient had any digitization points outside the range, it was rejected as a saturated pulse. A total of 579 saturated transients were found out of 4876 recorded files.

Two additional cuts on the individual transients were imposed, both applied simultaneously. As can be clearly seen in figure 4.4, the filtered LAr transient has two extrema, namely two minima, located around 2 μs and 3 μs. These features were used to determine the true LAr transients from false events, and the inverted transients occasionally observed. Every transient that passed the non-saturation criteria had

its pretrigger region average voltage $\langle V \rangle$ computed. Each of these was then digitally filtered and scanned to locate at what time value its minimum filtered pulse height occurred at. These minimal pulse heights were then converted into absolute pulse heights using the $c_0\langle V \rangle$ baseline shift as described in section 4.2. Scatter plots of these filtered pulse heights against their corresponding time channels were then plotted for all data sets. Figure 4.6 through 4.9 show these scatter plots for all four data sets. The vertical lines in the figure show the placement of the time channel cut. Any LAr transient that had its pulse height occurring in the time window between those two lines was accepted as a candidate for signal. Those events outside the lines were rejected as background. The spread in the time channel for the signal candidates is caused by the superposition of random electrical noise on the true LAr transient. There were a small number of unexplained inverted pulses in the data. They were also rejected by this method as the location of their filtered minima did not fall in the proper time window. It was found that the total number of inverted transients rejected was 178, and the total number of false triggers was 2399. Thus, a total of 3156 files out of a total number of 4876 were rejected by these initial cuts.

The filter design of this analysis provides one further advantage that can be clearly seen in figure 4.9; the data from the 2 mm cell. This figure shows a clustering of pulse heights around the 2 μs time channel. This corresponds to the secondary minimum that can be seen in figure 4.4. This secondary minimum is the result of the filter "seeing" the sharp fall time in the signal where the horizontal baseline suddenly jumps into the sharply downward sloping fall time of the LAr transient. Many of the LAr transients from the 2 mm cell had very small amplitudes, with some not being much higher in amplitude than the level of intrinsic noise. On filtering, it would be clear that some of the actual signal pulses could end up with filtered amplitudes less

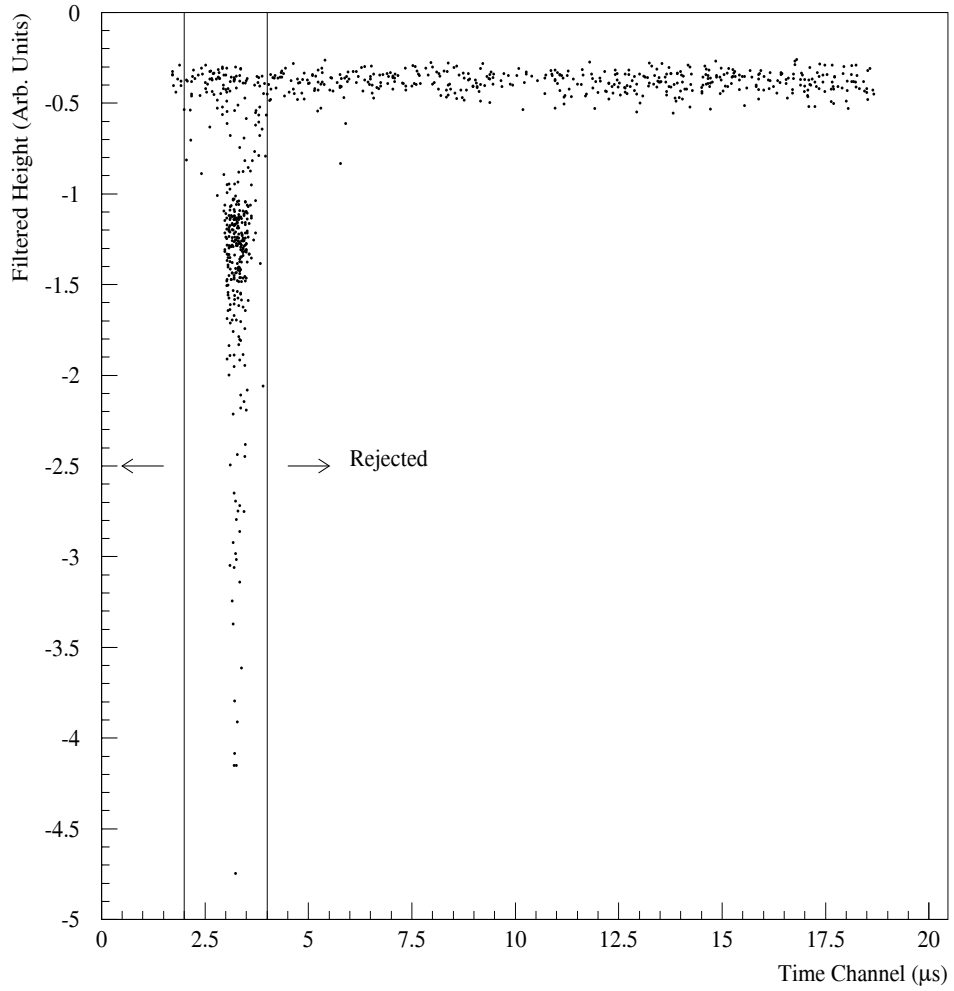

Figure 4.6: Scatter plot of filtered height distribution against time channel for 3 kV/cm data. The points contained in the vertical strip were accepted as signal transients; those outside the strip were rejected as false events or inverted pulses. The spread on the time channel is a result of random electrical noise.

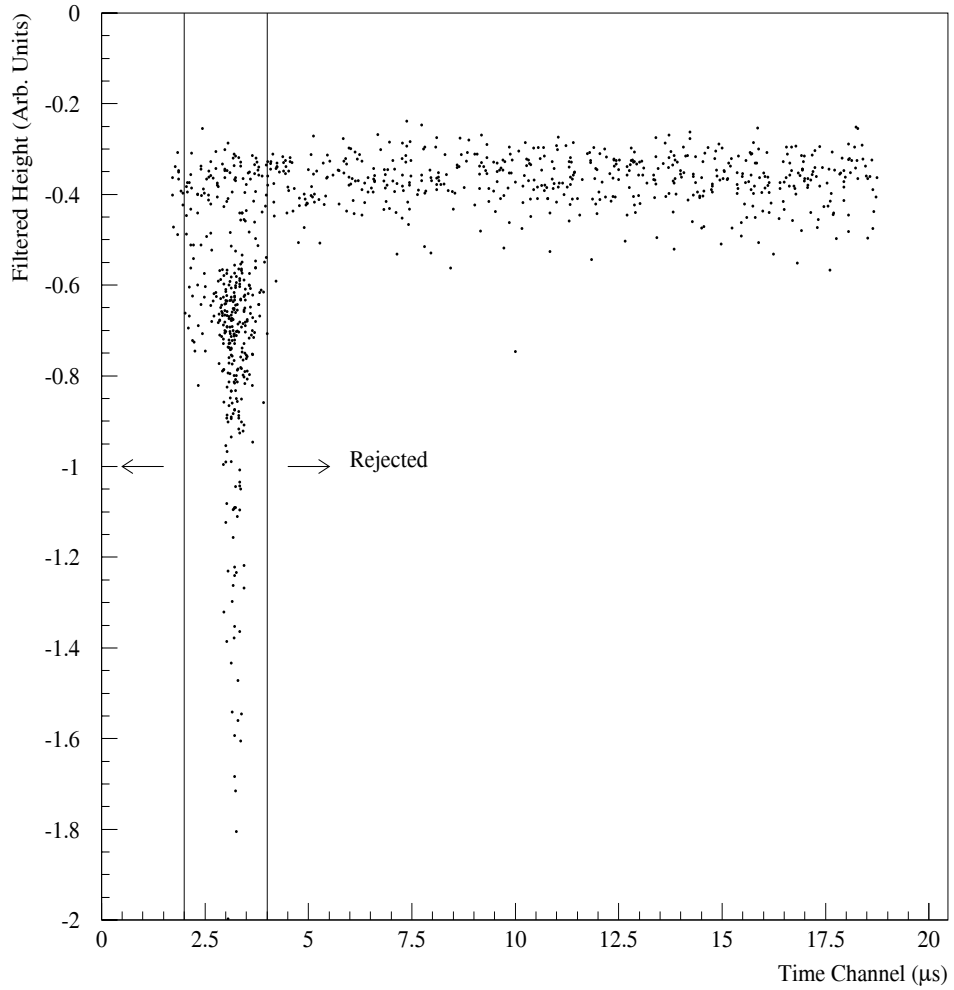

Figure 4.7: Scatter plot of filtered height distribution against time channel for 1 kV/cm data. The points contained in the vertical strip were accepted as signal transients; those outside the strip were rejected as false events or inverted pulses.

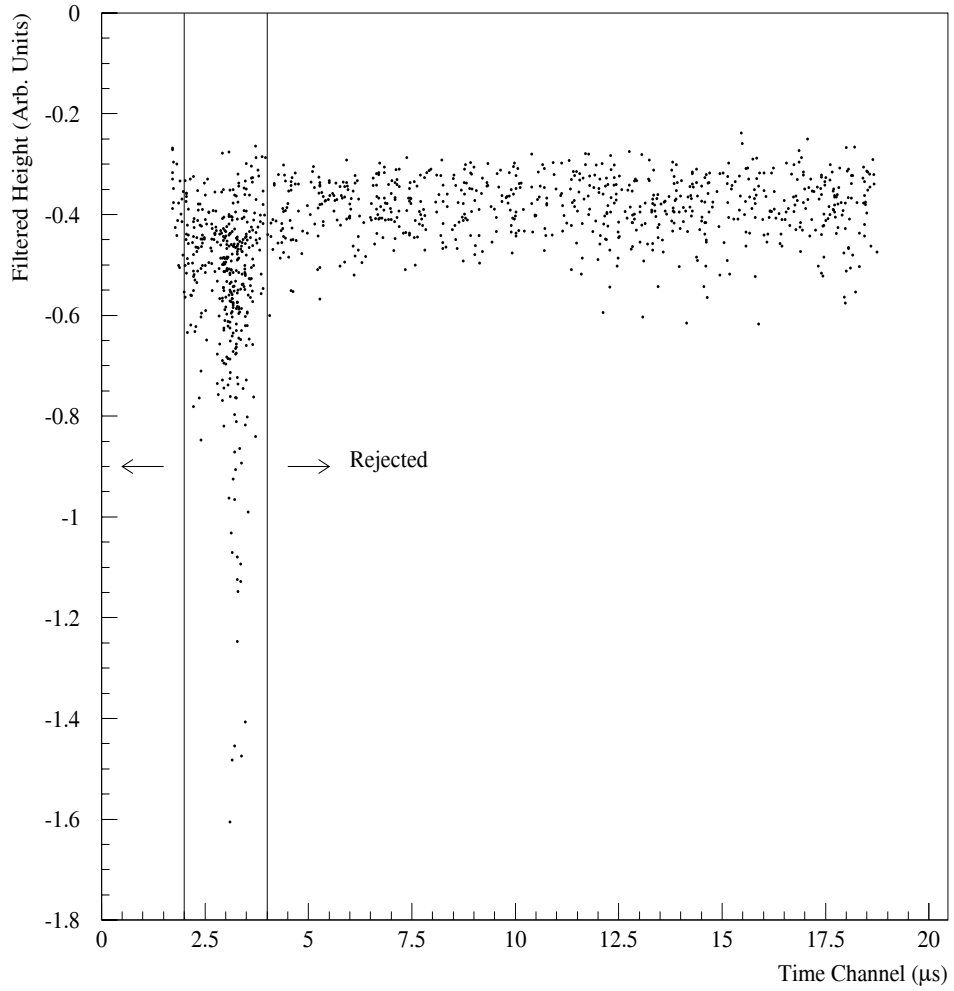

Figure 4.8: Scatter plot of filtered height distribution against time channel for 500 V/cm data. The points contained in the vertical strip were accepted as signal transients; those outside the strip were rejected as false events or inverted pulses.

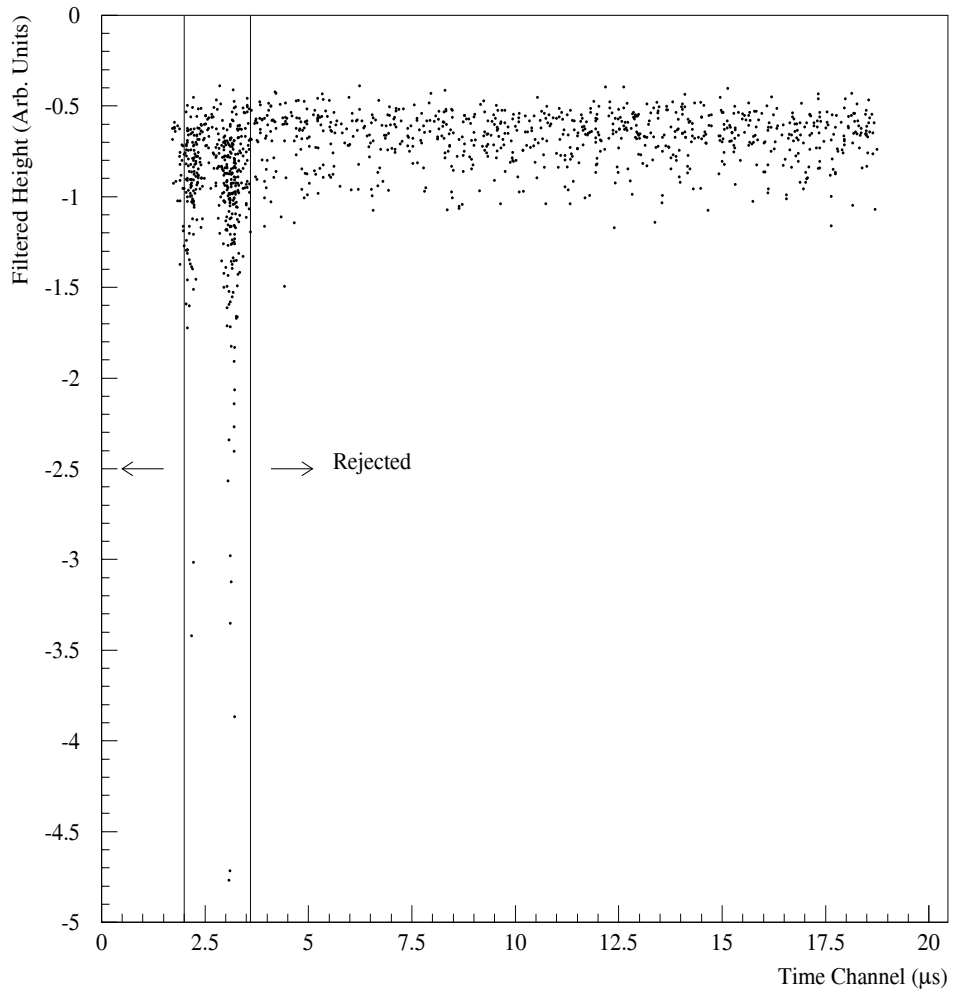

Figure 4.9: Scatter plot of filtered height distribution against time channel for the 3 kV/cm data from the 2 mm gap cell. The points contained in the vertical strip were accepted as signal transients; those outside the strip were rejected as false events or inverted pulses. Note the double band in the acceptance window: both strips are signal events.

in magnitude than that of the filtered noise. The design of this filter circumvents this by being sensitive to the sharp fall time at the trigger point, and can further distinguish signal from background using the feature of the secondary minimum.

4.5 Electron Lifetime Analysis

The transients passing the selection criteria of §4.4 were subject to one final filtered pulse height selection cut. The pulse height definition used in the following part of the analysis takes the value of the filtered transients at the fixed time channel corresponding to the theoretical location of the pulse minimum. In the cases of the 10.0 mm gap data for the 3 kV/cm, and the 1 kV/cm, pulse height histograms of the digitally filtered transients, passing the selection criteria of §4.4, were generated. Each histogram was scanned through in slices of pulse height value to find a lower limit on the filtered heights such that the few remaining background events surviving the cuts of §4.4 would be mostly eliminated. The procedure was one of choosing a lower limit on the filtered pulse height, and then using this cut, generate an averaged LAr transient from those files with filtered pulse height values greater than the value of the cut. In this way, the purity of the ensemble averaged LAr transient would be maximized. Figure 4.10 shows a pulse height histogram for the 10.0 mm gap, 3 kV/cm data. The peak below the pulse height value of 0.5 contains mostly noise events, and these were excluded from the ensemble averaged LAr transient for this data set.

The pulse height histograms of the other data sets did not exhibit a clearly defined noise peak, as in figure 4.10, where the noise files could be distinguished from the true events. In these cases, a lower cut off on the filtered pulse height was determined by trial and error testing of various lower limit values, and plotting out the ensemble averaged transient from those files with filtered heights below the lower cut off. The

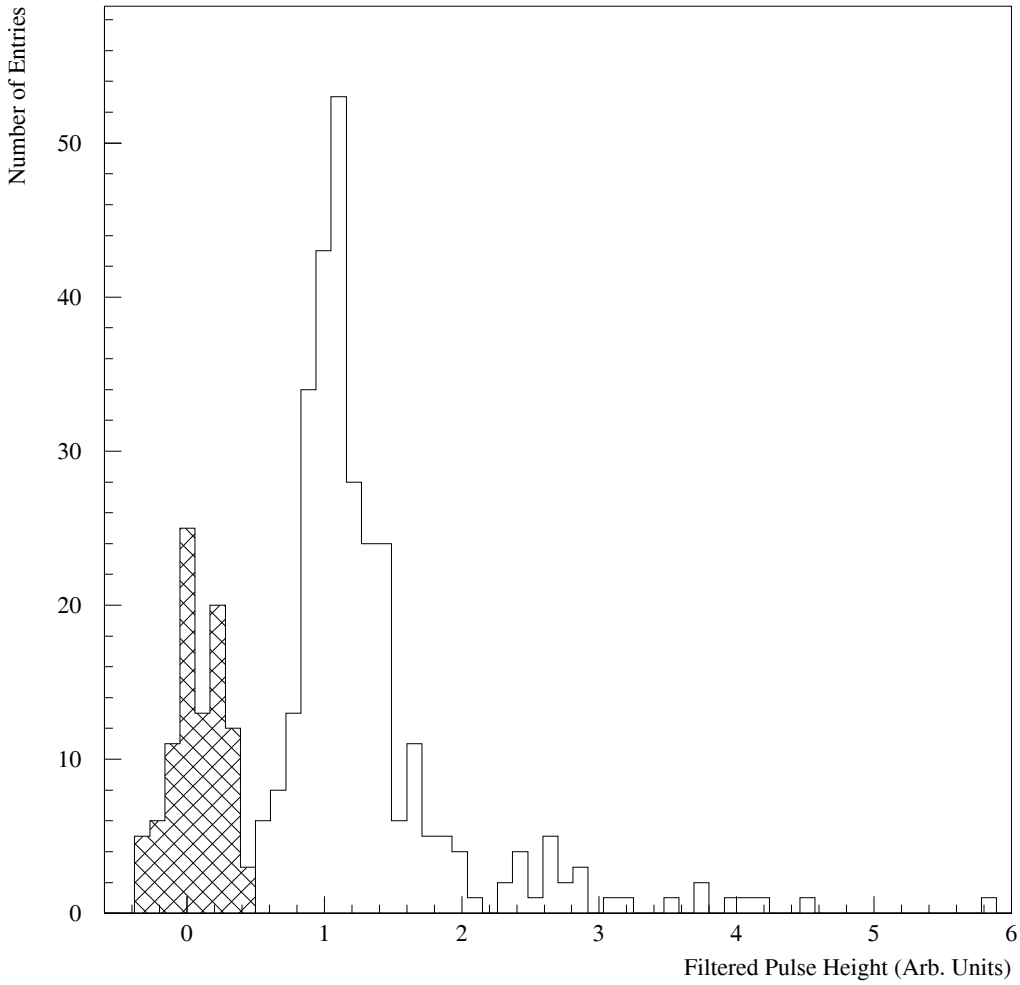

Figure 4.10: Histogram showing the filtered pulse height cut imposed on the 10.0 mm gap, 3 kV/cm data set. Events falling in the hatched region were excluded from the ensemble averaged LAr transient for this data set.

final value for the lower limit of the pulse height cut was determined when the visual level of the averaged transient signal degraded to a point where it was comparable to the visual level of noise. Figure 4.11 shows an example of this for the 10.0 mm

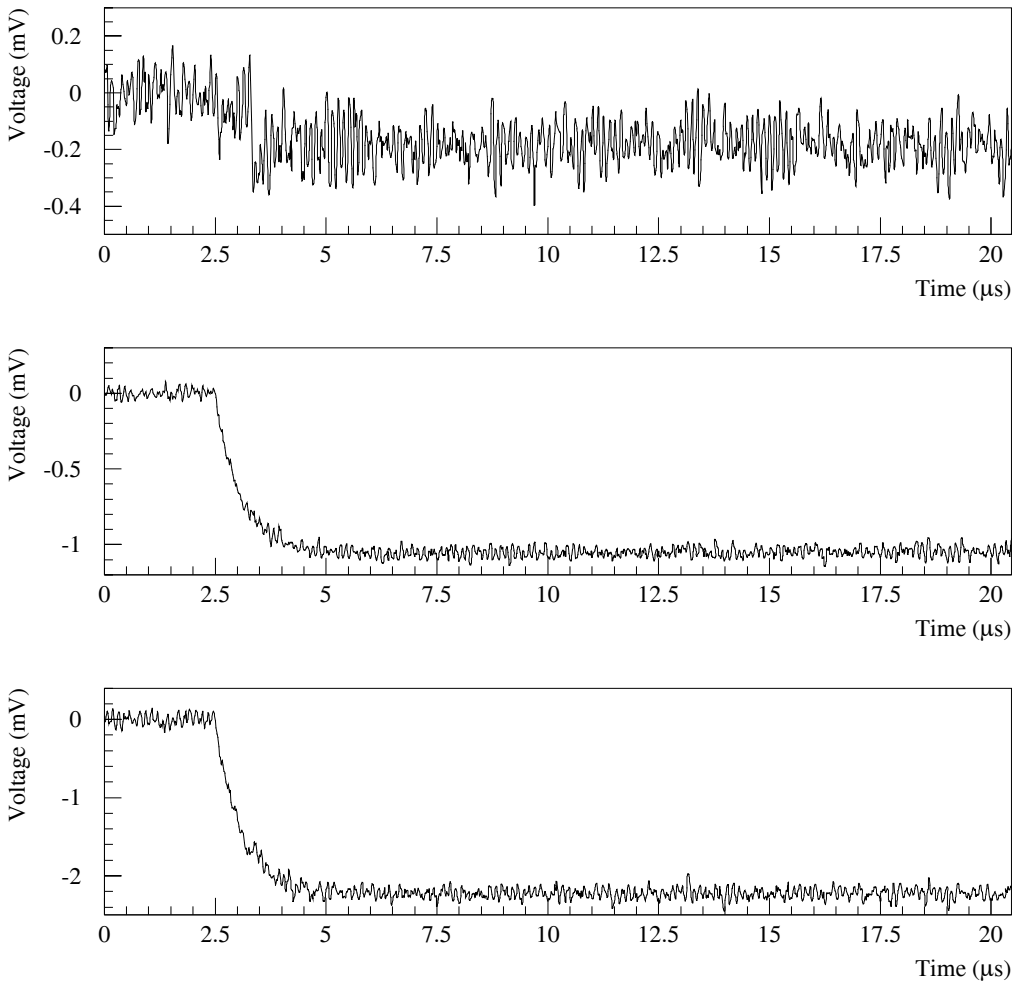

Figure 4.11: Intermediate ensemble averaged LAr transients for the 10.0 mm gap, 500 V/cm data set. The top portion shows the average transient for filtered pulse heights less than 4.9×10^{-2}, were noise is comparable to signal. The middle portion shows the average transient for filtered pulse heights between 4.9×10^{-2} and 4.8×10^{-1}. The lower portion shows the average transient for filtered pulse heights greater than 4.8×10^{-1}. Note the shape of the two lower transients match. Filtered pulse height values are quoted in arbitrary units.

gap, 500 V/cm data set. To ensure that this method was not biasing the shape of the LAr transient, and hence the result for τ_l, ensemble LAr transients for other slices in filtered pulse height values were generated from within the histogram, and visually compared in shape with each other to verify that the quantitative features of the shapes were preserved.

In this way, four unfiltered ensemble averaged LAr transients for each of the electric field settings used on the cells; namely 3 kV/cm, 1 kV/cm, and 500 V/cm for the 10.0 mm gap cell, and 3 kV/cm on the 2.0 mm gap cell, were generated. The final set of cuts used in the final generation of the ensemble averaged transients are summarized in table 4.3.

10.0 mm Gap Cuts		
Field	Time (μs)	FPH (Arb. Units)$\times 10^{-1}$
3 kV/cm	$2.0 \leq t \leq 4.0$	$\mid$ FPH $\mid \geq 5.0$
1 kV/cm	$2.0 \leq t \leq 4.0$	$\mid$ FPH $\mid \geq 2.5$
500 V/cm	$2.0 \leq t \leq 4.0$	$\mid$ FPH $\mid \geq 4.9 \times 10^{-1}$
2.0 mm Gap Cuts		
Field	Time (μs)	FPH (Arb. Units)$\times 10^{-1}$
3 kV/cm	$2.0 \leq t \leq 3.6$	$\mid$ FPH $\mid \geq 1.5$

Table 4.3: Summary of the final cuts imposed on all data sets. Here FPH = Filtered Pulse Height, and t is the digitized time channel value corresponding to $\mid$ FPH $\mid$.

The electron lifetime is found by fitting the four ensemble averaged LAr transients to equation 2.16. All four data sets can be fit simultaneously since the electron lifetime is not electric field dependent, and thus, common to all of the transients. In practice the fit also lets the starting time of each transient, known as the triggering position, to be determined by the fit. The drift time for each electric field and the overall normalization parameter, β, for each transient, are also included into the fit. It was

found that allowing the three drift times, t_d, to float produced physically unreasonable fit values for all three drift times, with t_d for 500 V/cm being shortest and t_d for 3 kV/cm being longest. For this reason the drift velocities for all field strengths were held fixed to nominal values from the literature [16]. Figure 4.12 shows some typical electron drift velocity curves as functions of electric fields for various LAr-gas mixtures. The electron drift velocities were parameterized by fitting the drift velocity values of the pure argon curve in figure 4.12, to a function of the form:

$$v_d(E) = P_1 E + P_2 E^{P_3} \text{ (m/s)}, \tag{4.5}$$

with $P_i\,, i = 1, 2, 3$, being the parameters of the fit, and E in units of kV/cm. The results of the P_i from the fit are:

$$\begin{aligned} P_1 &= -188.2 \pm 0.7 \\ P_2 &= 1747.5 \pm 0.6 \\ P_3 &= 0.5263 \pm 0.0004\,. \end{aligned}$$

The result of this fit is shown in figure 4.13. From the fit of equation 4.5, the drift velocities were held fixed at the values of: 2550 m/s, 1560 m/s, and 1190 m/s, for the 3.0 kV/cm, 1.0 kV/cm, and 500 V/cm data, respectively. Further to these constraints, a final constraint had to be imposed on the overall normalization parameter β, of equation 2.16. It was found during initial attempts to fit the transients that β, as a free parameter, could vary over several orders of magnitude, and MINUIT was still be able to find a solution within these extremes that would minimize the global χ^2 of the fits. It therefore became imperative that constraints be found for β to reduce the parameter space of the fits. Therefore, the right side of equation 2.16 was integrated

analytically from $t = 0\,\mu$s out to $t = 17.9\,\mu$s, to give a new function, $H(\tau_l, t_d)$,

$$H(\tau_l, t_d) = \beta \sum_{i=1}^{2} \int_0^{17.9} (\cdots)\, dt\ , \tag{4.6}$$

where the ellipses represent the functional expression of τ_l and t_d in the sum of equation 2.16. The data was numerically integrated using Simpson's 1/3 rule from $t = 2.56\,\mu$s out to $t = 20.46\,\mu$s, to give a purely numerical result denoted as $\mathcal{I}$. The numerical value of the integration is then equated to the expression in equation 4.6, and we then have for β,

$$\beta = \frac{\mathcal{I}}{\sum_{i=1}^{2} \int_0^{17.9} (\cdots)\, dt}\ . \tag{4.7}$$

The difference in limits of integration between the analytical integration and the numerical integration arises from the time axis shift in the data due to the trigger position. With this result, β is constrained in the fit to obey the functional dependence on τ_l and t_d as given in equation 4.7, with t_d fixed by the fixing of the drift velocities.

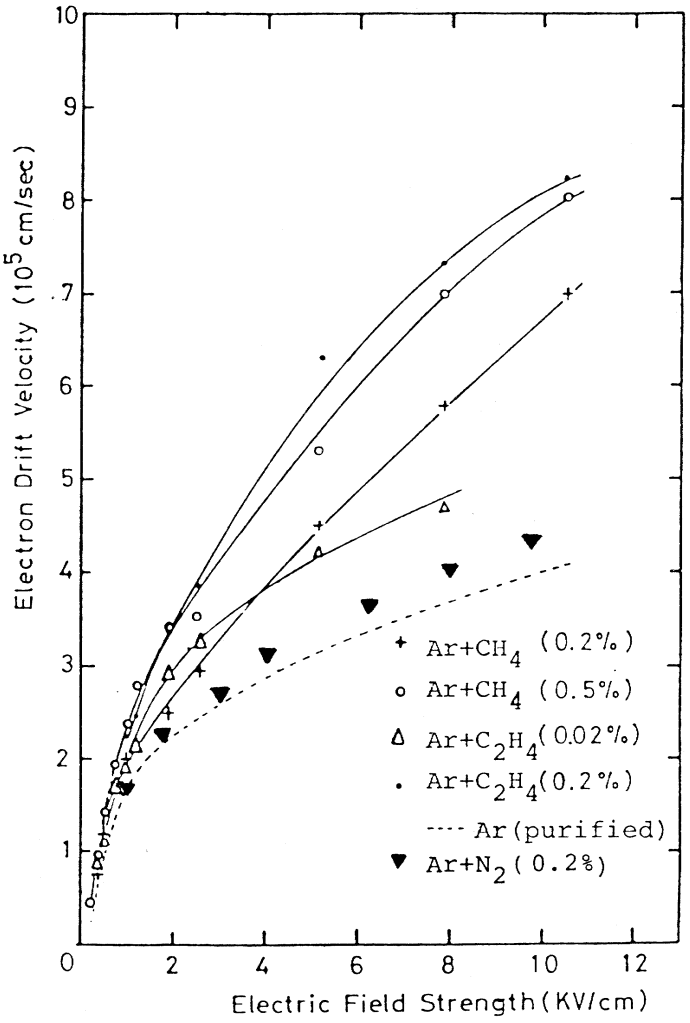

Figure 4.12: The variation of electron drift velocity as a function of the applied electric field, and for various types of contaminants. Source [16].

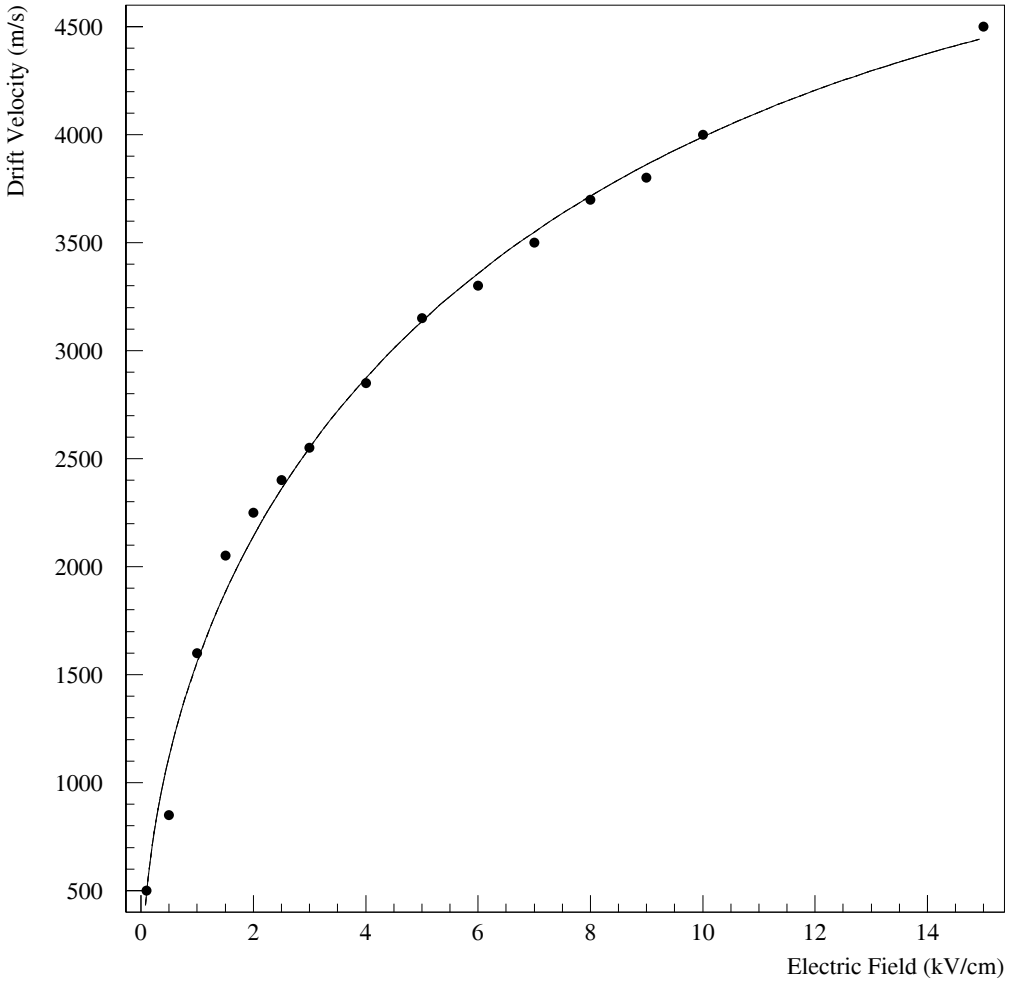

Figure 4.13: The fit of equation 4.5 to the pure LAr data points of reference [16]. The data points were read from the plot in figure 4.12.

Chapter 5

Results and Discussion

The results of the simultaneous fit of the four data sets of ensemble averaged LAr transients are summarized in table 5.1. The ensemble averaged LAr transient data, for each of the three electric fields used in this experiment, and the results of the fit are shown in figures 5.1 through 5.4.

Summary of Fit Results		
Gap (mm)	Field (kV/cm)	t_0 (DP)
10.0	3	126.6 ± 0.1
10.0	1	121.0 ± 0.2
10.0	0.5	117.3 ± 0.3
2.0	3	121.0 ± 0.2
$\tau_l = (0.897 \pm 0.005)\,\mu$s		

Table 5.1: Summary of the results of a chisquare minimization fit of the four LAr transients from this experiment. The trigger positions are quoted in digitization points. Multiply by $2.0 \times 10^{-3}\,\mu$s to obtain their equivalent time values.

The global χ^2/dof from the fit is 1.41 for 4087 total degrees of freedom. A plot of the χ^2 as a function of τ_l is shown in figure 5.5. As can be seen, there is a clear minimum in the plot located at the determined value for the electron lifetime. It is

found that the electron lifetime of this experiment is;

$$\tau_l = \left(0.897 \pm 0.005\ (\text{stat.})\ ^{+0.023}_{-0.032}\ (\text{syst.})\right)\mu\text{s}\,,$$

where the first error quoted is statistical, and the second error is systematic. The statistical error arises from the purely statistical result from MINUIT [15].

The dominant systematic affect in this analysis arises from the uncertainty in the electron drift velocities, as they were not allowed to be free in the fit. The uncertainty due to this effect was estimated by varying the drift velocity values by $\pm 20\%$ from the nominal values obtained from the fit of equation 4.5. The 20% variation was chosen to ensure ample coverage of the other data curves of figure 4.12. The values of τ_l that differed maximally above and below the fit value of τ_l were used for the upper and lower bounds on the quoted systematic uncertainty estimates. In each case it was found that the 3 kV/cm drift velocity variation caused the greatest changes in τ_l. These changes were found to range $^{+0.023}_{-0.032}$ away from the fit result for τ_l.

The characteristic time constants for the preamplifiers were also allowed to vary $\pm 3\sigma$ away from their nominal fit results, and it was found that τ_l differed maximally just 0.001 μs from its fit result. When added in quadrature with the systematic uncertainties from the drift velocity variations, the electronics systematic is negligible, leaving us with the final result of systematic uncertainty as stated in the above paragraph.

5.0.1 Consistency Check on The Fit

The result of the fit can be checked by making sure that the normalizations, β, give consistent values for the relative amount of charge collected between the two ionization cells at equal electric fields. Since the muon track length in the 10.0 mm

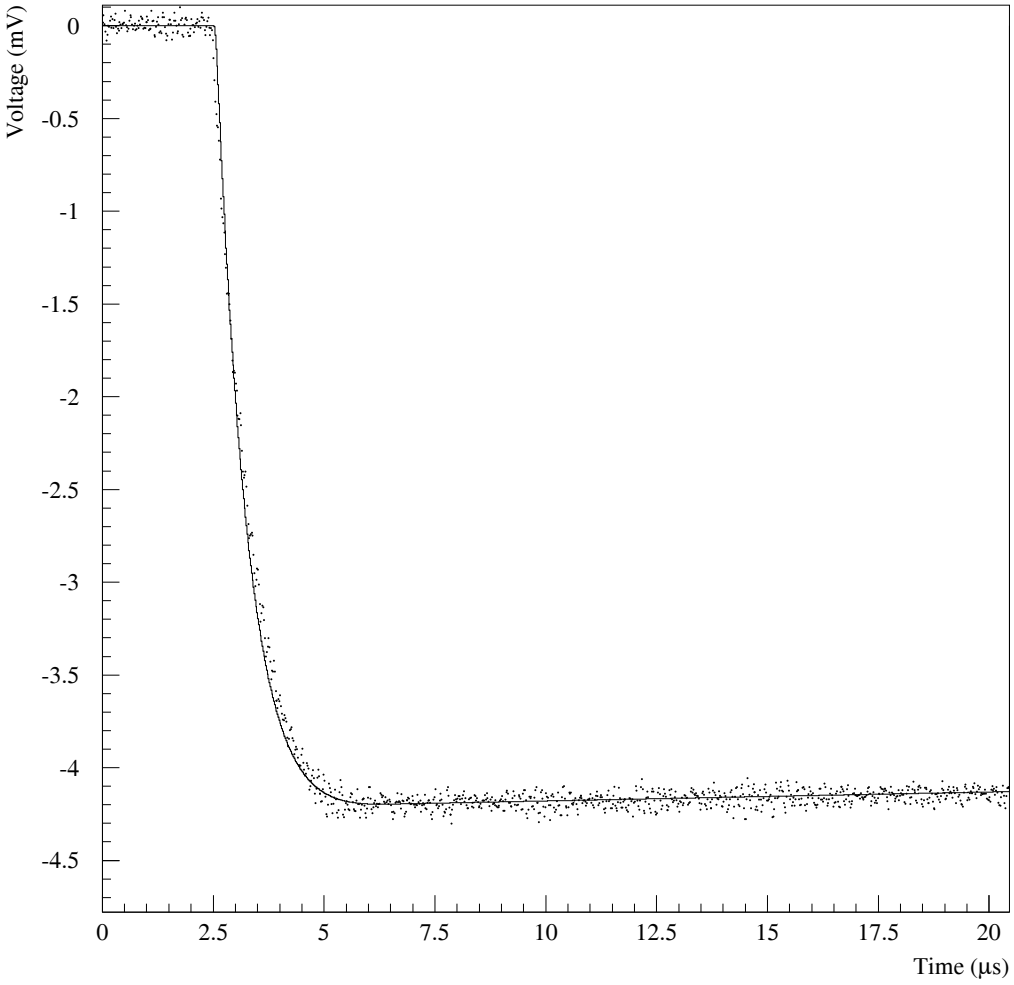

Figure 5.1: The ensemble average LAr voltage transient for the 3 kV/cm, 10.0 mm gap cell, with data shown as points, and the fit as the solid line.

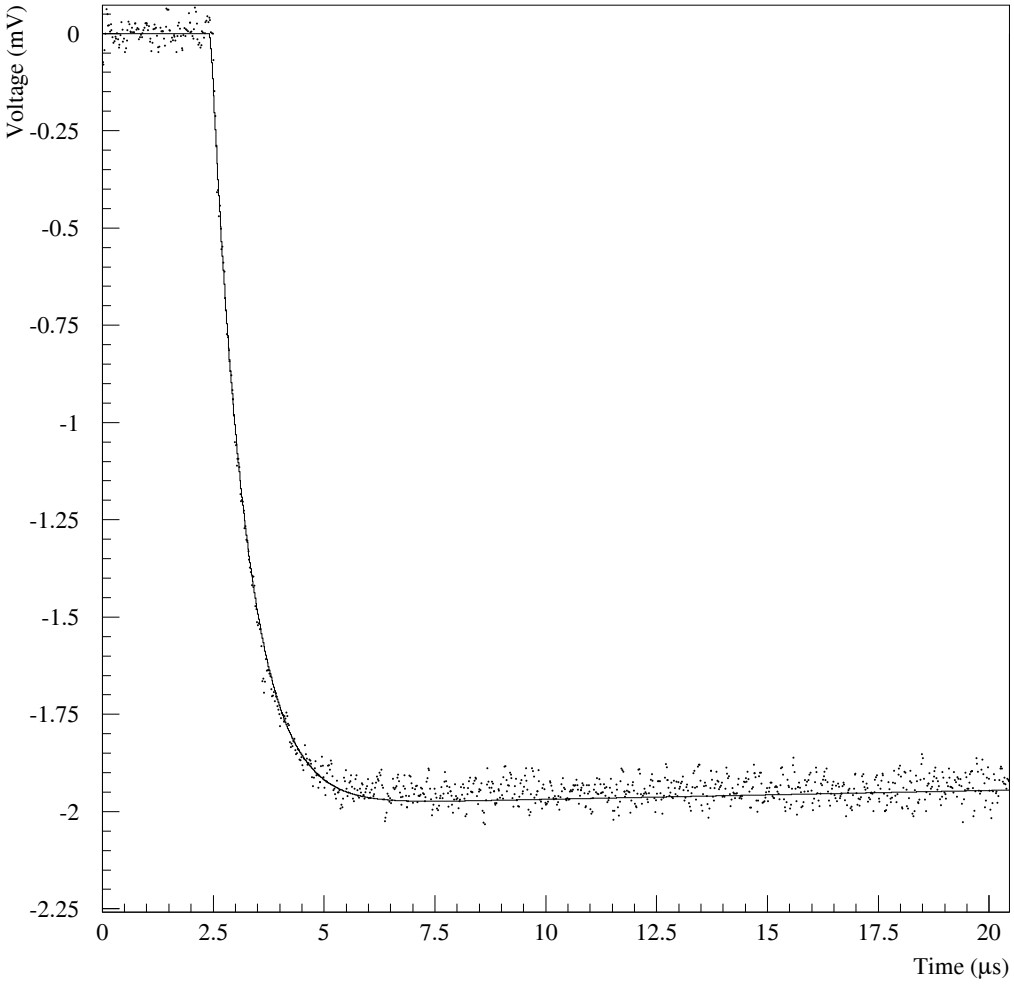

Figure 5.2: The ensemble average LAr voltage transient for the 1 kV/cm, 10.0 mm gap cell, with data shown as points, and the fit as the solid line.

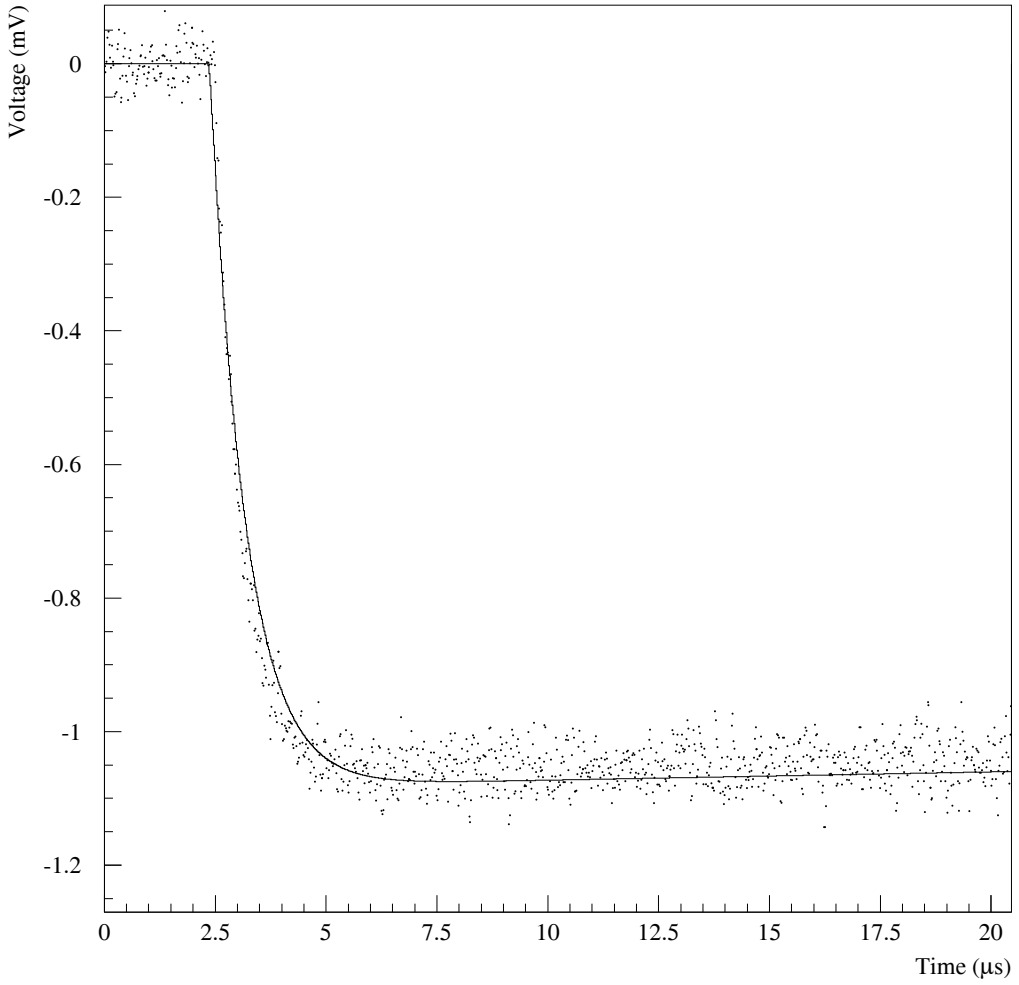

Figure 5.3: The ensemble average LAr voltage transient for the 500 V/cm, 10.0 mm gap cell, with data shown as points, and the fit as the solid line.

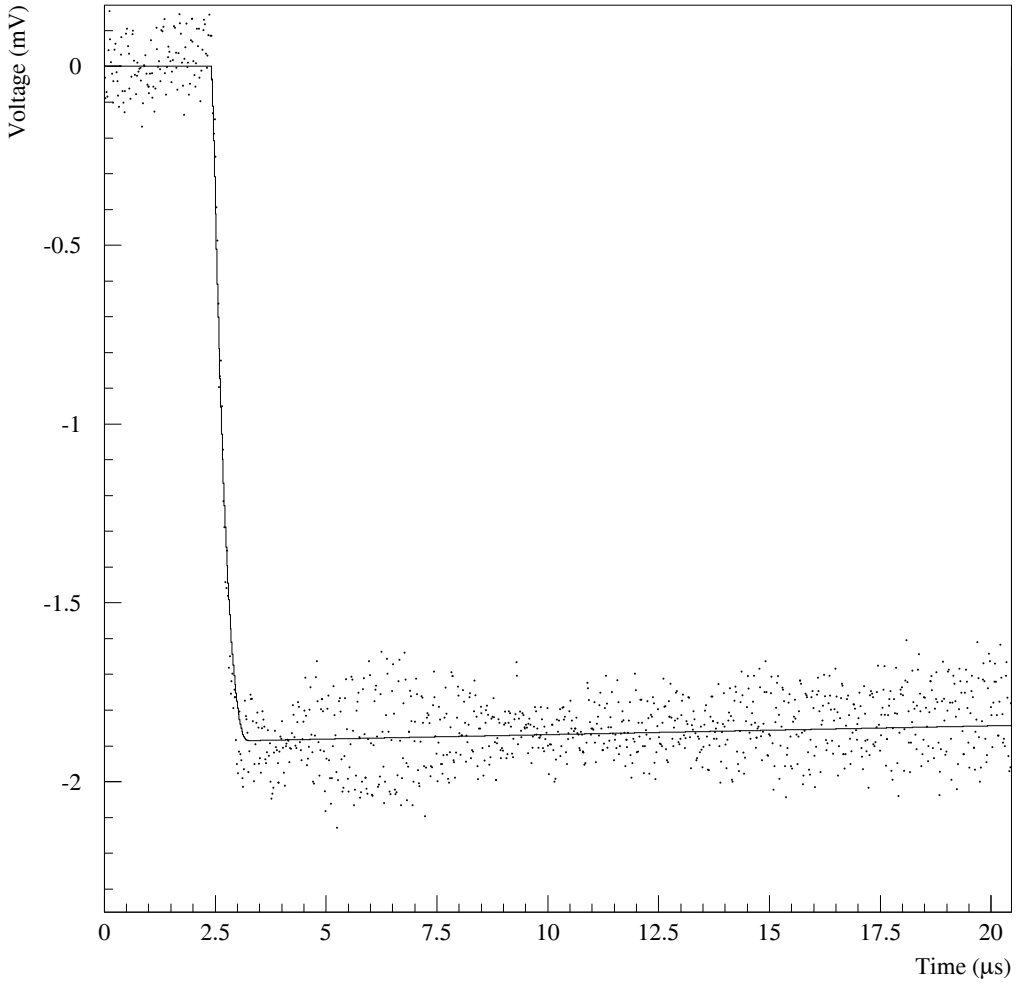

Figure 5.4: The ensemble average LAr voltage transient for the 3 kV/cm, 2.0 mm gap cell, with data shown as points, and the fit as the solid line.

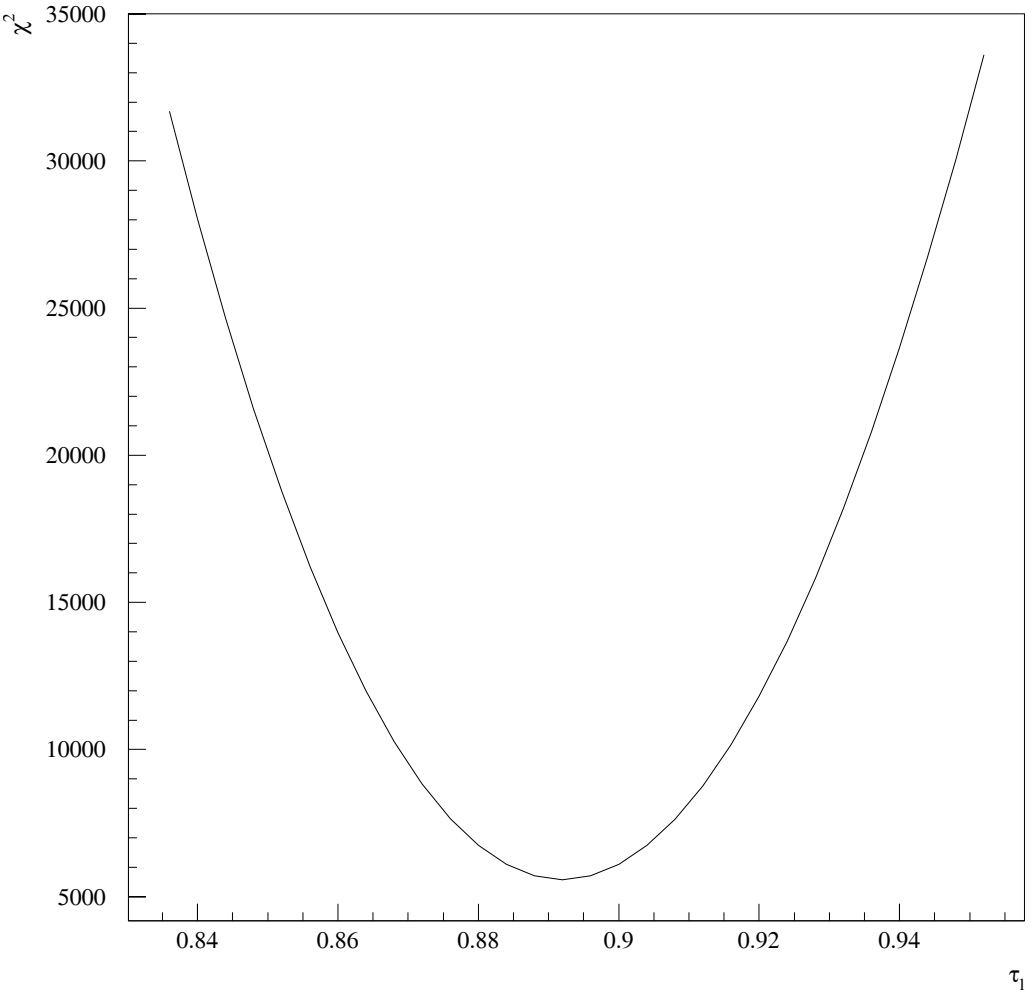

Figure 5.5: The χ^2 as a function of the free electron lifetime. The minimum defines τ_l.

gap ionization cell is five times longer than in the 2.0 mm gap cell, the signal, and hence, the average number of electrons, N, produced along the track length in the 10.0 mm gap, should be five times that of the 2.0 mm gap cell. We can determine the ratio of charge collected between the two ionization cells by analyzing the ratio of the their two respective β values determined from the fit.

From equation 2.17 we can obtain Ne/τ_3 for each ionization cell as:

$$G\frac{Ne}{\tau_3} = \beta\frac{(\tau_2 - \tau_1)}{\tau_2}\,, \tag{5.1}$$

where it is understood that for each ionization cell the electronics time constants, $\tau_{1,2}$, are different, due to the difference in preamplifiers, and τ_3 is identical to each, as it is the characteristic time constant of the oscilloscope. The right side of equation 5.1 is completely determined by the fit results. Therefore, taking the ratio of the right side of equation 5.1 for the 10.0 mm gap cell to that for the 2.0 mm gap cell will result in the ratio, R, of the average number of electrons collected between the 10.0 mm gap cell and the 2.0 mm gap cell, apart from a gain correction factor between the two preamplifiers used. We can express this result as,

$$R = \left(\frac{G^{10.0\,\mathrm{mm}}}{G^{2.0\,\mathrm{mm}}}\right)\left(\frac{N^{10.0\,\mathrm{mm}}}{N^{2.0\,\mathrm{mm}}}\right)\,. \tag{5.2}$$

The gain correction factor for the two preamplifiers was determined by injecting delta "spike" voltage pulses into each preamplifier, and obtaining a total of twenty output impulse response files for each preamplifier. Each set of 20 was averaged into an overall output pulse for each preamplifier. The ratio between the absolute maximum pulse height from each resulting averaged output pulse determined the gain factor. By this method, it was found that the gain ratio between the two preamplifiers

was,

$$\frac{G^{2.0\,\mathrm{mm}}}{G^{10.0\,\mathrm{mm}}} = 1.12 \pm 0.02\,, \tag{5.3}$$

where the error is absolute and represents the RMS noise in each averaged output pulse. Multiplying the result of equation 5.2 by the result of equation 5.3 will correct R for the difference in preamplifiers.

A final correction to the ratio of the average charge produced between the two ionization cells, R, is required because the ionization deposited within each cell is dE/dx dependent. As shown in equation 2.21, the number of electrons produced from initial ionization is proportional to the energy deposition per unit length, dE/dx, of the ionizing particle. As a result of this, the amount of charge produced will be slightly different in the 2.0mm gap cell, as it sits atop the the 10.0mm gap cell.

This correction was done in the following manner: The total amount of material that a muon would be required to pass through, common to both cells, includes the lower three parallel plates of the cell arrangement, the amount of liquid argon sitting below the level of the top cell plate, and finally, the material of the cryo-cooler. We approximate the cryo-cooler as a uniform slab of steel, with equivalent mass of the cooler, and of $10\,\mathrm{cm} \times 10\,\mathrm{cm}$ in area; the same area as the scintillators. With this simple approximation, the equivalent depth of steel the muons would have to pass through representing the cryo-cooler would be approximately 19.6 cm. From nuclear range data tables, converted for muons as discussed in §2.3.1, it is found that the minimum energy required for a muon to pass through the material common to both cells is $\approx 301\,\mathrm{MeV}$. For the dE/dx correction factor to R, we take the muon kinetic energy at the centre of the 2.0 mm gap cell, that is after traversing through 1.0 mm of liquid argon, and also the corresponding kinetic energy of the muon at the centre of the

10.0 mm gap cell, and then determine from the converted dE/dx tables approximate values for dE/dx at these locations. We assume these values will be close to the total averaged change in dE/dx for each cell. This is a reasonable assumption as our dE/dx values are right around the minimum ionization point of figure 2.6 where the curve is very flat. The values are found to be approximately 2.28 MeV/cm, and 2.19 MeV/cm for the 2.0 mm and 10.0 mm gap cells, respectively. The ratio of the 10.0 mm dE/dx value to the 2.0 mm dE/dx value is ≈ 0.96. It is this factor we correct R by. With this and the gain correction factor, the final result we obtain for R is,

$$R = 5.17 \pm 0.10 \text{ (stat.)} \, ^{+0.76}_{-0.54} \text{ (syst.)} \, .$$

consistent with the expected value of five, with the first error quoted is statistical and the second being systematic, and both are absolute. The statistical error represents the contribution from the gain factor correction. The estimate on the systematic error of R is discussed below. Note that the errors in this quote have been adjusted accordingly for the dE/dx correction. This result shows that the integration of the data, as discussed in §4.5, is an effective means to eliminate the problem of MINUIT being able to find a fit to the data for values in β ranging over several orders of magnitude.

The systematic error quoted for the ratio of average charge collected between the two ionization cells at 3 kV/cm was obtained by the $\pm 20\%$ variation in the electron drift velocities. It was found that R varied maximally with the variations on the 3 kV/cm drift velocity. The result is $^{+0.76}_{-0.54}$. Varying the characteristic time constants for both preamplifiers by $\pm 3\sigma$ revealed that R changed as much as 0.004 in value from the quoted fit result. Adding this result in quadrature with the drift velocity systematic uncertainties gives an estimated systematic uncertainty on R of $^{+0.76}_{-0.54}$.

5.0.2 O_2 Equivalent Contamination

For electric field strengths less than 5 kV/cm, it has been empirically shown [7] that the concentration of oxygen equivalent impurities, $[O_2]$ in liquid argon can be expressed as,

$$[O_2] = \gamma \frac{E\ (\mathrm{kV/cm})}{\lambda\ (\mathrm{cm})}\,[\mathrm{ppm}], \tag{5.4}$$

where E is the electric field strength, and $\lambda = v_d \tau_l$ is the mean free path for the absorption of the free electrons by the impurities, and γ is a constant of proportionality determined as $(0.15 \pm 0.03)\ \frac{\text{ppm-cm}}{\text{kV/cm}}$ [7]. The field strength of 0.5 kV/cm is the lowest field strength used that will provide the most accurate result for $[O_2]$, because the drift time is the longest. The value of the lifetime obtained in this work corresponds to a mean free path of $(1.07 \pm 0.01\ (\text{stat.}) \pm 0.21\ (\text{syst.}))$ mm at 500 V/cm. Here, the statistical error arises from the statistical contribution from the electron lifetime, and the systematic error is the result of the $\pm 20\%$ variation on the drift velocity added in quadrature with the systematic result from the electron lifetime. With this, we find that the concentration of oxygen equivalent impurities in this experiment to be,

$$[O_2] = \left(748 \pm 150\ (\text{stat.})\ ^{+186}_{-125}\ (\text{syst.})\right)\ [\text{ppb}]\,,$$

with the first error quoted being statistical, arising from errors in the mean free path added in quadrature with the quoted error in the value of γ.

The systematic error on the O_2 level of contamination, was determined by holding all parameters fixed at their fit values, and varying only the values for the 500 V/cm drift velocities. These were varied $\pm 20\%$ from nominal. The error values quoted express the difference between the nominal fit result and those obtained with the 500 V/cm drift velocity variation. It was found that the concentration of oxygen equivalent contamination varied $^{+186}_{-125}$ from the fit result by this method.

The 3σ electronic time constant variation produced a maximal change in $[O_2]$ of only 0.001 [ppb]. When added in quadrature this contribution is negligible, leaving the systematic uncertainty as that quoted above.

Chapter 6

Conclusions

A liquid argon ionization chamber was constructed and operated using a specially modified cryo-cooler apparatus. A system designed to damp mechanical vibrations, and decouple the ionization cell from their effects, was shown to perform well; allowing data to be acquired using only a single charge integrating preamplifier. A self-contained cryogenic system allowed condensing of the liquid argon, and maintaining it at a controlled temperature of 86 K over the course of the experimental run. A measurement of the free electron lifetime in liquid argon was made, by way of voltage transient analysis, using cosmic ray muons as the source of ionization.

The vibrational damping system reduced the acoustic noise levels sufficiently so that no shaping electronics were required in the analog data acquisition circuit. This was a significant improvement over previous efforts [1, 17]. In principle, this will allow for more precise measurements of the electronic properties of liquid argon. Unfortunately, the increased sensitivity caused by these efforts brought to bear that the mathematical model of the preamplifiers used in this experiment was inadequate. However, the increased levels of sensitivity attained should allow for using a broad band amplifier in any future experiments.

We have determined the free electron lifetime in this experiment to be,

$$\tau_l = \left(0.897 \pm 0.005\ (\text{stat.})\ ^{+0.023}_{-0.032}\ (\text{syst.})\right)\mu\text{s}\,,$$

and the concentration of oxygen equivalent contamination in the liquid argon as,

$$[O_2] = \left(748 \pm 150\ (\text{stat.})\ ^{+186}_{-125}\ (\text{syst.})\right)\ [\text{ppb}]\,.$$

The uncertainty in the free electron drift velocities is what clearly dominates the systematic uncertainty in the results. Past measurements of the type done in this work [1, 17] did not encounter this difficulty, however, these measurements included an additional timing filtering amplifier in the data acquisition circuit that dominated signal shaping. This suggests that the inability to allow the drift velocities to be free in the fit could possibly be attributed to the poorly modelled impulse response behaviour of the preamplifiers. Improved performance of the electronics could well increase the sensitivity to the amount of oxygen equivalent contamination to better than 200 [ppb].

Future work could focus on making measurements of the drift velocity of electrons in liquid argon. For example a time of flight measurement using a parallel plate photocathode, could be done by directing laser light of the appropriate frequency onto the cathode, liberating electrons, with negligible initial velocities, into the gap between the two electrodes. An alternative to this method would be to allow ionizing particles from a beam line to traverse horizontally between the electrodes, at known distances from a given electrode determined by silicon strip detectors placed at each end of the cell. Employing the same measuring technique as described above, and knowing the electron drift distance as determined by the silicon strip detectors, would also allow for a direct measurement of the electron drift velocities at various electric fields across the cell gap.

Bibliography

[1] P. R. Schenk, *Transient Analysis of Electrons Drifting in Liquid Argon*, University of Victoria, 1989.

[2] L. J. Geis, *Transform Analysis and Filters*, Prentice Hall (1989)

[3] G. N. Fowler and A.W. Wolfendale, *The Hard Component of μ-Mesons in the Atmosphere*, in *Encyclopedia of Physics Volume XLVI/1*, Springer-Verlag, Berlin, (1961).

[4] W. R. Leo, *Techniques for Nuclear and Particle Physics Experiments*, Springer-Verlag, Berlin, (1987)

[5] Particle Data Group, *Particles and Fields*, Physical Review D54 (1996), 123.

[6] International Commission on Radiation Units and Measurements *Stopping Powers and Ranges for Protons and Alpha Particles*, ICRU Report 49, 1993.

[7] W. Hofmann, *et al.*, *Production and Transport of Conduction Electrons in a Liquid Argon Ionization Chamber*, Nuclear Instruments and Methods, 135 (1976) 151-156.

[8] George F. Simmons, *Differential Equations with Applications and Historical Notes*, McGraw Hill (1991)

[9] A. Astbury, *et al.*, *The Electronic Response of 2,2,4,4 Tetramethylpentane to Minimum Ionizing Particles*, Nuclear Instruments and Methods, A305 (1991) 376.

[10] APD Cryogenics Inc. Model DE-204SL.

[11] E. Butkov, *Mathematical Physics*, Addison-Wesley, 1968.

[12] R.W. Hamming, *Digital Filters*, Prentice Hall, New Jersey, 1989.

[13] Centorr Model 2B-20-Q

[14] H. Gotoh and H. Yagi, *Solid Angle Subtended by a Rectangular Slit*, Nuclear Instruments and Methods, 96 (1971) 485-486.

[15] F. James and M. Roos, MINUIT - Function Minimization and Error Analysis, CERN Computer Centre Program Library (1989).

[16] T. Doke, *Fundamental Properties of Liquid Argon, Krypton and Xenon as Radiation Detector Media*, Portugal Phys., 12 (1981) pp557.

[17] Y. Li, *The Electronic Response of 2,2,4,4 Tetramethylpentane to Minimum Ionizing Particles*, University of Victoria, 1990.

[18] J. D. Jackson, *Classical Electrodynamics*, John Wiley & Sons, New York, 1975.

[19] David J. Griffiths, *Introduction to Electrodynamics*, Prentice Hall, New Jersey, 1981.

[20] W. Smythe, *Static and Dynamic Electricity*, McGraw-Hill Book Co., New York, 1950, p. 34.

Appendix A

Digital Filters

The aim of this section is to provide a brief review of the theory and construction of digital filters. For further insight, the reader is recommended to look into Hamming's book *Digital Filters* [12].

The underlying cause of a signal and its associated noise is generally different. Therefore, the frequency spectrum of the signal and the noise are also different and hence, there may be the possibility to enhance the signal relative to the noise by filtering the signal in an appropriate frequency band. Consequently, it is customary to work in the frequency domain of the signal under interest. Doing this then lends itself to understanding how one wants to construct a filter in frequency space that will act appropriately on those frequencies associated with the signal.

A.1 Some Definitions

A non-recursive digital filter (DF) is is a linear formula into which is fed a sequence of measured inputs, $u_n(t)$, such that an output, $y_n(t)$ is produced through the formula,

$$y_n(t) = \sum_{k=-\infty}^{\infty} c_k u_{n-k}(t). \tag{A.1}$$

Here, the c_k are called the filter coefficients, and most importantly, the $u_n(t)$ are all *sampled at equal time intervals*, usually by virtue of the equally spaced time sampling performed by the ADC.

In practice, we must truncate the filter to a finite number of terms, say N of them. Additionally, if the coefficients are odd in the index k so that $c_{-k} = -c_k$ then we will have for our filter,

$$y_n = c_0 u_n + \sum_{k=1}^{N} c_k (u_{n-k} - u_{n+k}). \tag{A.2}$$

A.2 Aliasing and the Nyquist Interval

Defined in words, aliasing is the phenomenon where *sampled* points on a high frequency wave form are exactly matched in value to the sampled points of a wave form with a lower frequency. One says that the high frequency values are aliased down into a lower frequency. Because of this effect, we need only consider frequencies that lie within the Nyquist interval of $[(-1/2)f_{samp}, (1/2)f_{samp}]$, where f_{samp} is our sampling frequency. How does this work?

The oscilloscope samples the input wave form at integral multiples of some time interval, Δt. Now, consider the time signal sampled at the nth time value,

$$u(t_n) = \cos[2\pi(m + \alpha)n + \delta], \tag{A.3}$$

where m is an integer, α is the positive fractional part of the original frequency into which we absorbed the overall multiple of Δt, and δ is an arbitrary phase angle.

Because m and n are integers, we can write without change,

$$u(t_n) = \cos[2\pi\alpha n + \delta].$$

If $\alpha < 1/2$ then we are done; the frequencies of the original wave form have been aliased into the frequency interval of $[(-1/2)f_{samp}, (1/2)f_{samp}]$, where $f_{samp} = 1/\Delta t$. If $\alpha > 1/2$, then we can remove another $-2\pi n$ from the argument, and use $\cos(x) = \cos(-x)$ to get, $u(t_n) = \cos[2\pi(1-\alpha)n+\delta]$. And so, again, we have aliased the sample points into the Nyquist interval. Thus, when dealing with digitally sampled data, is it necessary to know the sampling rate at which the data were taken. The Nyquist frequency is then defined by one half of the original sampling frequency. Figure A.1 shows the aliasing between two waveforms, the high frequency one being of the form, $u(t) = \cos[2\pi(7/3)t - \pi/3]$, and its Nyquist counterpart, $u(t) = \cos[2\pi(1/3)t - \pi/3]$.

A.3 Digital Filters and Fourier Series

From the previous section we see, from the effect of aliasing, that sinusoid functions are the natural choice for fitting the sampled points of our original input sinusoid function.

Bearing this in mind then, consider an input to the filter of equation A.1 of the form, $u_n = e^{i\omega n}$. Then we will have,

$$y_n = e^{i\omega n} \sum_{k=-\infty}^{\infty} c_k e^{-i\omega k} = \lambda(\omega) e^{i\omega n}. \tag{A.4}$$

The result is an eigenvalue equation, with the digital filter from equation A.1 acting as the operator on the 'vector', $e^{i\omega n}$, producing the eigenvalue $\lambda(\omega) = \sum c_k e^{-i\omega k}$. We call $\lambda(\omega)$ the transfer function. As is well known from the theory of Fourier series, any well behaved continuous function $g(\omega)$ on the interval $[-\pi, \pi]$ can be expanded in terms of complex exponentials [11], so that,

$$g(\omega) = \sum_{k=-\infty}^{\infty} d_k e^{i\omega k}, \tag{A.5}$$

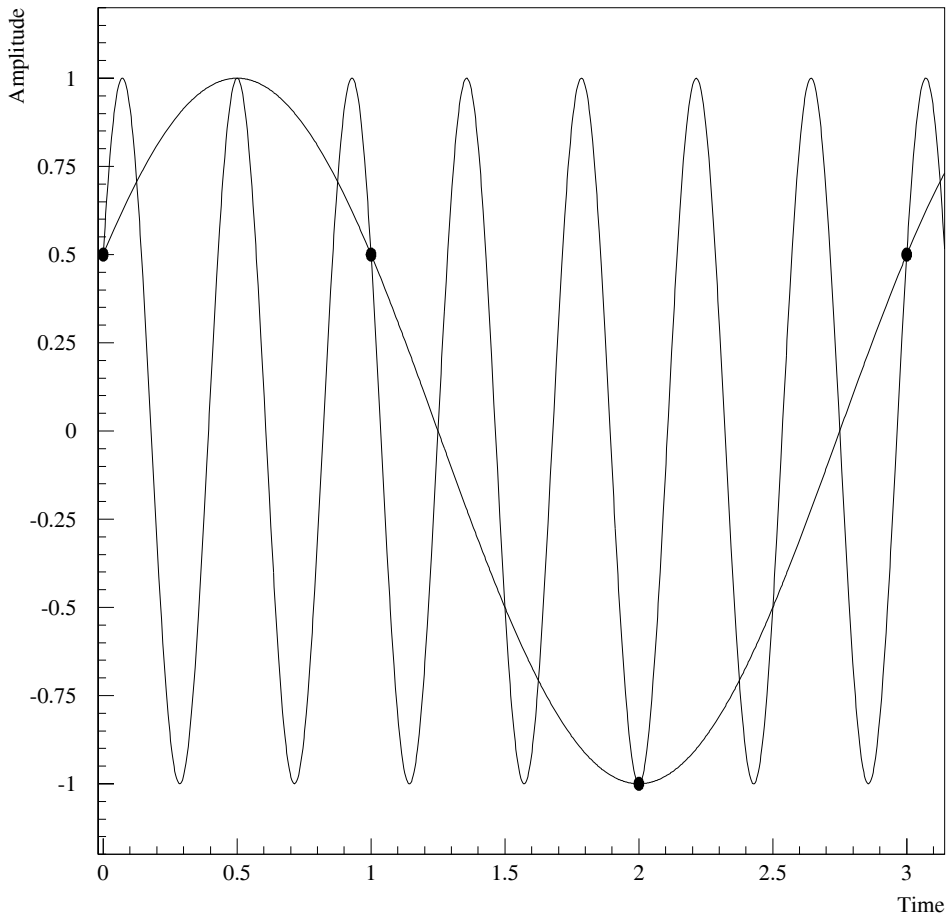

Figure A.1: The effect of aliasing. The sample points (integer multiples of time) of the high frequency wave form are aliased down to match at the same time points of the lower frequency wave form.

with coefficients d_k given by,

$$d_k = \frac{1}{2\pi} \int_{-\pi}^{\pi} g(\omega) e^{-i\omega k} d\omega. \tag{A.6}$$

If the coefficients d_k in equation A.6 are symmetric in k then the sum in A.5 can be

written as,

$$g(\omega) = \sum_{k=-\infty}^{\infty} d_{-k} e^{-i\omega k} \tag{A.7}$$

which upon comparison with the sum in equation A.4, with $c_k = d_{-k}$, shows that the coefficients of our digital filter are the Fourier coefficients of our transfer function. We can therefore calculate the coefficients of a digital filter by determining the Fourier coefficients of the transfer function.

A.4 Constructing a Bandpass Filter

The analytical bandpass filter is described by,

$$\lambda(f) = \begin{cases} 0 & , 0 \leq f < f_{low} \\ 1 & , f_{low} \leq f \leq f_{up} \\ 0 & , f_{high} < f < f_{nyq}, \end{cases} \tag{A.8}$$

where f_{nyq} is the Nyquist frequency of our sampling, and f_{low} and f_{up} are, respectively, the lower and upper cutoff frequencies of the bandpass window. As this function is even over the entire Nyquist interval, its Fourier expansion will involve only cosine terms. The Fourier expansion coefficients, c_n of λ on the Nyquist interval of $[-f_{nyq}, f_{nyq}]$ are found to be,

$$c_n = \frac{2}{n\pi} \left[\sin\left(\frac{n\pi f_{up}}{f_{nyq}}\right) - \sin\left(\frac{n\pi f_{low}}{f_{nyq}}\right) \right], \tag{A.9}$$

With these coefficients in equation A.4, we have for our Fourier expansion of the filter, $\lambda(f)$,

$$\lambda(f) = \frac{f_{up} - f_{low}}{f_{nyq}} + \sum_{n=1}^{\infty} c_n \cos\left(\frac{n\pi f}{f_{nyq}}\right), \tag{A.10}$$

which then must be truncated to a finite number of terms for practical use; 86 in total in the case of this work. In addition, these coefficients are odd in the index n, so the filter is of the form given in equation A.2.

Figure 4.3 shows what $\lambda(f)$ looks like for the sum up to $N = 85$ terms. Also, included in the figure is a plot of $\lambda'(\omega)$, which is the same truncated series, smoothed by using Lanczos σ factors [12], given by $\sigma(N, n) = \frac{\sin(\pi n/N)}{(\pi n/N)}$, such that the new filter coefficients c'_n become, $c'_n = \sigma(N, n)c_n$. By smoothing, it can be clearly seen that the undesirable oscillations in the truncated filter are significantly reduced. In this way, the smoothed filter has an amplitude that does not fluctuate as much around the value of 1, and so, the frequencies of interest passing through the filter will be preserved in their magnitudes, suffering little attenuation.

Appendix B

Noise and Digital Filters

It is well known from analogue electronics theory and practice that active filters in a circuit can be used to improve the output signal to noise ratio. In the same way, for digital signals a digital filter can also be employed to improve output signal to noise.

In this appendix an analytical expression for the transmission of noise through a digital filter is derived.

B.1 Some Definitions

For the purposes of the following mathematics it is important to set up some definitions to make the mathematical statements to follow more concise and easier to follow.

Let us define the expectation operator, $\mathcal{E}\{\nu_n\}$, to represent the operation of averaging over the ensemble of values ν_n. Clearly the expectation operator acting on a constant is just the constant back again. Further, because the nature of electrical noise, ϵ_n the noise amplitude, is random we can immediately conclude, by definition, the following two statements:

$$\mathcal{E}\{\epsilon_n\} = 0 \tag{B.1}$$

$$\mathcal{E}\{\epsilon_n \epsilon_m\} = \begin{cases} \sigma^2, & \text{for } m = n \\ 0, & \text{otherwise} \end{cases} \tag{B.2}$$

where σ^2 is the characteristic value of the variance on the measurements of the signal.

With these results in place we can go on to derive the expression for the transmission of noise through a digital filter.

B.2 Noise Transmission Formula

Suppose we have a digital signal represented by the inputs u_n. In addition, let there be a noise signal superimposed on this signal ϵ_n, so that our input to the digital filter takes on the form $u_n \mapsto u_n + \epsilon_n$. Then our output for the case of a general digital filter will be given by,

$$y_n = \sum_{k=-N}^{N} c_k (u_n + \epsilon_n) \tag{B.3}$$

With the aid of B.1, the expectation value, for y_n is just,

$$\mathcal{E}\{y_n\} = \sum_{k=-N}^{N} c_k u_n \,, \tag{B.4}$$

as one would expect.

For the variance, Var on the filtered signal we have,

$$\begin{aligned} \text{Var} &= \mathcal{E}\{\,[\,y_n - \mathcal{E}\{y_n\}\,]^2\,\} \\ &= \mathcal{E}\left\{\,[\,\textstyle\sum_{k=-N}^{N} c_k \epsilon_{n-k}\,]^2\,\right\} \\ &= \mathcal{E}\left\{\,\textstyle\sum_{k=-N}^{N}\sum_{l=-N}^{N} c_k c_l \epsilon_{n-k}\epsilon_{n-l}\,\right\} \\ &= \textstyle\sum_{k=-N}^{N}\sum_{l=-N}^{N} c_k c_l\, \mathcal{E}\{\,\epsilon_{n-k}\epsilon_{n-l}\,\} \\ &= \sigma^2 \textstyle\sum_{k=-N}^{N} c_k^2 \end{aligned} \tag{B.5}$$

where B.2 is used for the last step.

Therefore, the root mean square noise allowed through by a digital filter is finally given by the square root of the final line of B.5.

Appendix C

Induced Charge on a Parallel Plate Cell

C.1 Green's Reciprocation Theorem

The statement of Green's Reciprocation Theorem [18, 19, 20], states that for any two arbitrary systems, S and S', the following result holds true:

$$\int_{V'} \phi\rho'\, dV' + \oint_{A'} \phi\sigma'\, dA' = \int_{V} \phi'\rho\, dV + \oint_{A} \phi'\sigma\, dA. \tag{C.1}$$

where ϕ, ϕ', and σ, σ' and ρ, ρ', are the potentials, surface charge densities, and volume charge densities, for systems S and S', respectively. It is understood that the surface integrals are to be carried out over all conducting surfaces, A_i, of each system.

This powerful result relates all of the fundamental electrostatic quantities of two completely different, and independent, systems to each other. With this result, we will derive the ionization induced surface charge on the parallel plate cell of this experiment.

C.2 The Induced Charge

Let us choose as our two physical systems for the application of equation C.1 the following two systems: system S comprising two grounded infinite parallel plates

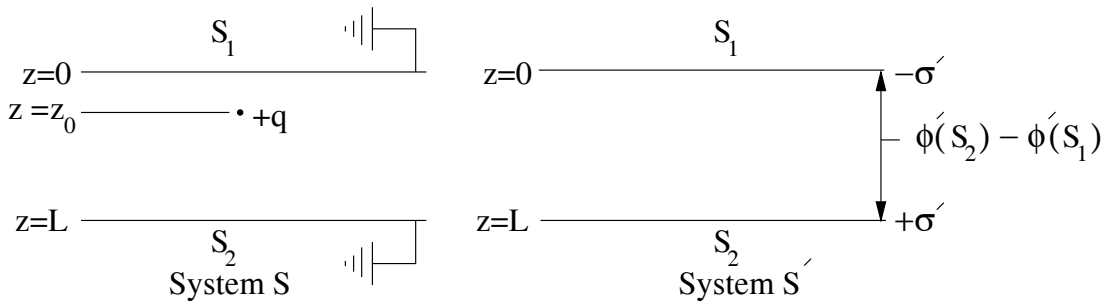

Figure C.1: The two systems Green's reciprocation theorem is being applied to. On the left is system S, and on the right is system S'.

with a point charge $+q$ at a distance z_0 from the top plate, and system S' comprising another parallel plate system with each plate carrying equal but opposite surface charge density σ, with no charge density between them, as shown in figure C.1.

With this choice of systems, we see that the left side of equation C.1 is clearly zero as there is no potential between the two grounded plates in system S to give rise to ϕ. Further, as these systems both have cylindrical symmetry, we have for ρ:

$$\rho = q\delta(z - z_0) \; . \tag{C.2}$$

With this charge density, the volume integral on the right side of equation C.1 reduces trivially to $q\phi'(z_0)$.

The surfaces of the plates are equipotentials, and so ϕ' is constant on these surfaces and can come out of the surface integrals in equation C.1. Denote the fact that ϕ' is being evaluated on each surface by, $\phi'(S_1)$ and $\phi'(S_2)$, for surfaces S_1 and S_2, respectively. Finally, we note that the total induced charge q_i on each plate S_i for $i = 1, 2$ is given by:

$$q_i = \oint_{S_i} \sigma_i \, dS_i \tag{C.3}$$

and that to conserve charge over all we must have

$$q_1 + q_2 + q = 0\,,$$

leads us to be able to reduce equation C.1 to

$$\begin{aligned} q[\ \phi'(S_2) - \phi'(z_0)\ ] + q_1[\ \phi'(S_2) - \phi'(S_1)\ ] &= 0 \\ \Rightarrow q_1 &= q\tfrac{\phi'(S_2)-\phi'(z_0)}{\phi'(S_1)-\phi'(S_2)} \end{aligned} \tag{C.4}$$

The electric field between the plates in system S' from the surface charge density σ is just

$$\vec{E} = \frac{\sigma}{\epsilon_0}\hat{z}\,, \tag{C.5}$$

where $\hat{z}$ is the unit vector that points in the positive z direction. With this we find that the difference in potentials, as stated in equation C.4, give as the induced charge on S_1,

$$q_1 = +q\left(\frac{z_0}{L} - 1\right)\ . \tag{C.6}$$